

# Turbulent dynamo in the two-phase interstellar medium

Amit Seta <sup>★</sup> and Christoph Federrath

*Research School of Astronomy and Astrophysics, Australian National University, Canberra, ACT 2611, Australia*

Accepted XXX. Received YYY; in original form ZZZ

## ABSTRACT

Magnetic fields are a dynamically important component of the turbulent interstellar medium (ISM) of star-forming galaxies. These magnetic fields are due to a dynamo action, which is a process of converting turbulent kinetic energy to magnetic energy. A dynamo that acts at scales less than the turbulent driving scale is known as the turbulent dynamo. The ISM is a multiphase medium and observations suggest that the properties of magnetic fields differ with the phase. Here, we aim to study how the properties of the turbulent dynamo depend on the phase. We simulate the non-isothermal turbulent dynamo in a two-phase medium (most previous work assumes an isothermal gas). We show that the warm phase ( $T \geq 10^3$  K) is transsonic and the cold phase ( $T < 10^3$  K) is supersonic. We find that the growth rate of magnetic fields in the exponentially growing stage is similar in both phases. We compute the terms responsible for amplification and destruction of vorticity and show that in both phases vorticity is amplified due to turbulent motions, further amplified by the baroclinic term in the warm phase, and destroyed by the term for viscous interactions in the presence of logarithmic density gradients in the cold phase. We find that the final ratio of magnetic to turbulent kinetic energy is lower in the cold phase due to a stronger Lorentz force. We show that the non-isothermal turbulent dynamo is significantly different from its isothermal counterpart and this demonstrates the need for studying the turbulent dynamo in a multiphase medium.

**Key words:** magnetic fields – ISM: magnetic fields – dynamo – methods: numerical

## 1 INTRODUCTION

The interstellar medium (ISM) of galaxies is a dynamic medium between stars consisting of thermal gas, dust, magnetic fields, and cosmic rays. The thermal gas in the ISM is turbulent with turbulence being driven at a range of scales by a number of mechanisms including stellar outflows, supernova explosions, and gravitational instabilities (Elmegreen & Scalo 2004; Scalo & Elmegreen 2004; Mac Low & Klessen 2004; Elmegreen 2009; Federrath et al. 2017; Krumholz et al. 2018). This turbulence amplifies magnetic fields via a dynamo mechanism, the process of converting the kinetic energy of turbulence to magnetic energy, and generates multi-scale magnetic fields (Brandenburg & Subramanian 2005; Federrath 2016; Rincon 2019; Shukurov & Subramanian 2021). The density and temperature of the ISM gas vary over a range due to various heating and cooling processes (Sutherland & Dopita 1993). This leads to a multiphase structure in the ISM (Field et al. 1969; McKee & Ostriker 1977; Cox 2005; Ferrière 2020), where the physical processes and properties differ between the phases. For example, the stars are formed in cold, dense small volume filling regions and the hot, diffuse gas occupies a large volume of the ISM. The other components of the ISM such as turbulence, magnetic fields, and cosmic rays also show differences between the phases. Turbulence is expected to be subsonic (or transsonic) in the hot phase of the ISM and supersonic in the cold phase (Gaensler et al. 2011; Seta & Federrath 2021b; Federrath et al. 2021). Magnetic fields are observed to be stronger in

the denser regions of the ISM in comparison to the diffuse medium (Heiles & Troland 2005; Beck 2016). Cosmic rays (away from their sources) diffuse in the hot, ionised phase of the ISM but can propagate much faster in the cold, neutral medium (Cesarsky & Kulsrud 1981; Zweibel 2017; Farber et al. 2018; Beattie et al. 2022). Overall, the ISM is a multiphase, turbulent plasma and in this paper, we primarily study how the magnetic field amplification and properties differ between the ISM phases.

Magnetic fields are an important component of the ISM of star-forming galaxies. They provide additional support against gravity (Boulares & Cox 1990), heat up the gas via magnetic reconnection (Raymond 1992), alter the gas flow (Shetty & Ostriker 2006), reduce the efficiency of star formation (Federrath 2015), control the propagation of cosmic rays (Cesarsky 1980; Shukurov et al. 2017), affect galactic outflows (van de Voort et al. 2021), and might also play a role in the galaxy’s evolution (Pakmor & Springel 2013). Thus, it is important to study the strength, structure, and evolution of magnetic fields in galaxies.

Observationally, magnetic fields in nearby spiral galaxies can be studied using radio polarisation observations. Based on these observations, magnetic fields can be divided into large- and small-scale components. The large-scale component is probed via the Faraday rotation measure and polarised synchrotron emission, whereas the small-scale component is studied using the fluctuations in the Faraday rotation measure and the level of depolarisation (Sokoloff et al. 1998; Haverkorn 2015; Beck 2016). Usually, in star-forming galaxies, the observed small-scale random magnetic fields are stronger than the large-scale component (see Table 3 in Beck et al. 2019). In

<sup>★</sup> E-mail: amit.seta@anu.edu.au

the nearby spiral galaxy, M51, the large-scale radio polarisation observations, which probe the hot (and warm), diffuse phase of the ISM, show different magnetic field properties (especially the magnetic field structure) than that seen via the recent large-scale far-infrared polarisation observations, which probe the cold, dense phase (Fletcher et al. 2011; Borlaff et al. 2021). In the Milky Way, the large-scale magnetic field properties inferred from OH masers (a probe of the colder regions) and that from pulsars (a probe of warmer regions) are different (Ogbodo et al. 2020). Even on the smaller scales in the Milky Way, magnetic fields in the warm and cold medium can be different (Campbell et al. 2021). Thus, observationally, the properties of both the small- and large-scale magnetic fields differ in different phases of the ISM.

Dynamo theory is used to study the strength, structure, and evolution of magnetic fields in galaxies. Based on the driving scale of turbulence ( $\sim 100$  pc in a typical spiral galaxy), dynamos can also be divided into two types: the turbulent/fluctuation or small-scale (which amplifies magnetic fields with correlation length less than the driving scale of turbulence) and mean field or large-scale (amplifying magnetic fields at scales greater than the driving scale of turbulence, i.e., several kpcs in a typical spiral galaxy)<sup>1</sup>. The turbulent dynamo, which is due to the random stretching of magnetic field lines by the turbulent velocity, quickly amplifies weak seed magnetic fields (Subramanian 2016) and saturates due to back-reaction of the growing magnetic fields on the turbulent flow (Kazantsev 1968; Vainshtein & Zel'dovich 1972; Zel'dovich et al. 1984; Kulsrud & Anderson 1992; Subramanian 1999, 2003; Schekochihin et al. 2004; Haugen et al. 2004; Brandenburg & Subramanian 2005; Federrath et al. 2011, 2014; Seta et al. 2020; McKee et al. 2020; Seta & Federrath 2021a). The saturated turbulent dynamo generated magnetic field then seeds the mean field dynamo (Ruzmaikin et al. 1988). Besides turbulence, the mean field dynamo also needs large-scale galaxy properties such as differential rotation, shear, and density stratification to order and amplify magnetic fields over galaxy scales (Krause & Rädler 1980; Ruzmaikin et al. 1988; Beck et al. 1996; Brandenburg & Subramanian 2005; Shukurov & Sokoloff 2008). Even theoretically, from the dynamo theory, we would expect the magnetic field properties to differ with the ISM phase because of different turbulence properties (e.g., the compressibility of the medium). Here, we primarily focus on the turbulent dynamo in a two-phase medium to explore the magnetic field properties in different phases.

Almost all studies of the turbulent dynamo assume turbulence in an isothermal gas (except Gent et al. 2021, which simulates multiphase gas in a supernova-driven turbulence setup but they do not distinguish dynamo properties based on phases). In this work, we use driven turbulence numerical simulations with a heating and cooling prescription for the gas to explore the turbulent dynamo in a two-phase medium. We aim to study how the properties of the turbulent dynamo and the magnetic field it generates depend on the phase of the medium.

In Sec. 2, we describe our numerical methods and parameters for non-isothermal turbulent dynamo simulations. Then, in Sec. 3, we discuss the properties of the two-phase, turbulent medium. We determine and discuss the dependence of the turbulent dynamo on the phase of the medium in Sec. 4. Finally, we summarise and conclude our results in Sec. 5.

<sup>1</sup> The ‘large-’ and ‘small-’ scales defined based on the driving scale of turbulence (usually in theory and simulations) can be different than that used in the observations.

## 2 NUMERICAL METHODS

### 2.1 Basic equations

To study the turbulent dynamo in non-isothermal plasmas, we use a modified version of the FLASH code (version 4, Fryxell et al. 2000; Dubey et al. 2008) to numerically solve the equations of non-ideal compressible magnetohydrodynamics. We use the HLL3R (3-wave approximate) Riemann solver (Waagan et al. 2011) to solve the following equations on a uniform, triply periodic cartesian grid with  $512^3$  grid points:

$$\frac{\partial \rho}{\partial t} + \nabla \cdot (\rho \mathbf{u}) = 0, \quad (1)$$

$$\frac{\partial (\rho \mathbf{u})}{\partial t} + \nabla \cdot \left( \rho \mathbf{u} \otimes \mathbf{u} - \frac{1}{4\pi} \mathbf{b} \otimes \mathbf{b} \right) + \nabla p_{\text{tot}} = \nabla \cdot (2\nu \rho \boldsymbol{\tau}) + \rho \mathbf{F}_{\text{dri}}, \quad (2)$$

$$\frac{\partial \mathbf{b}}{\partial t} = \nabla \times (\mathbf{u} \times \mathbf{b}) + \eta \nabla^2 \mathbf{b}, \quad \nabla \cdot \mathbf{b} = 0, \quad (3)$$

$$\frac{\partial e_{\text{tot}}}{\partial t} + \nabla \cdot \left( e_{\text{tot}} + p_{\text{tot}} \mathbf{u} - \frac{1}{4\pi} (\mathbf{b} \cdot \mathbf{u}) \mathbf{b} \right) = \rho \mathbf{u} \cdot \mathbf{F}_{\text{dri}} + n_{\text{H}} \Gamma - n_{\text{H}}^2 \Lambda(T) + 2\rho \nu |\boldsymbol{\tau}|^2 + \frac{\eta}{4\pi} (\nabla \times \mathbf{b})^2, \quad (4)$$

where  $\rho$  is the density,  $\mathbf{u}$  is the velocity field,  $\mathbf{b}$  is the magnetic field,  $p_{\text{tot}} = p_{\text{th}} + (1/8\pi)|\mathbf{b}|^2$  is the total pressure (sum of thermal,  $p_{\text{th}}$ , and magnetic pressures),  $\tau_{ij} = (1/2)(u_{i,j} + u_{j,i} - (2/3)\delta_{ij}\nabla \cdot \mathbf{u})$  is the traceless rate of strain tensor,  $\mathbf{F}_{\text{dri}}$  is the prescribed acceleration field for driving turbulence (see Sec. 2.3),  $\nu$  is the constant viscosity,  $\eta$  is the constant resistivity,  $e_{\text{tot}} = \rho e_{\text{int}} + (1/2)\rho|\mathbf{u}|^2 + (1/8\pi)|\mathbf{b}|^2$  is the total energy density (sum of internal,  $e_{\text{int}}$ , kinetic, and magnetic energy densities),  $n_{\text{H}}$  is the number density ( $= \rho/\mu m_{\text{H}}$ , where  $\mu = 1$  is the mean molecular weight and  $m_{\text{H}}$  is the mass of hydrogen),  $\Gamma$  is the constant heating rate,  $T$  is the temperature of the gas, and  $\Lambda(T)$  is the temperature dependent cooling function (see Sec. 2.2 for details of heating and cooling). We close the MHD equations with an equation of state of an ideal monatomic gas, i.e.,  $p_{\text{th}} = (\gamma_{\text{g}} - 1)\rho e_{\text{int}}$ , where  $\gamma_{\text{g}} = 5/3$  is the adiabatic index.

### 2.2 Heating and cooling prescription

Various mechanisms can heat or cool the gas in the ISM, depending on the temperature and density of the medium (Sutherland & Dopita 1993). For compressible turbulence, the density varies significantly and thus these processes can heat or cool the gas locally, which in turn can change the properties of turbulence and magnetic fields. We use a constant heating rate ( $\Gamma$ ) and a temperature dependent cooling function ( $\Lambda(T)$ ) of the form (Koyama & Inutsuka 2000, 2002)

$$\Gamma = 2 \times 10^{-26} \text{ erg s}^{-1}, \quad (5)$$

$$\frac{\Lambda(T)}{\Gamma} = \left[ 10^7 \exp\left(\frac{-1.184 \times 10^5}{T + 1000}\right) + 1.4 \times 10^{-2} T^{1/2} \exp\left(\frac{-92}{T}\right) \right] \text{ cm}^3, \quad (6)$$

where  $T$  is the temperature in Kelvin. These functions are constructed such that they describe the typical heating and cooling processes in a Milky Way type star-forming galaxy. We compute an equilibrium temperature by balancing heating and cooling functions, i.e.,  $\Gamma = n_{\text{H}}\Lambda$ . If the cooling or heating is very fast, the gas approaches the equilibrium temperature exponentially quickly (Vázquez-Semadeni et al. 2007; Mandal et al. 2020). This is referred to as the equilibrium cooling model (see Appendix A for further discussion and

comparison with the non-equilibrium cooling model). We also set a lower temperature floor of 2 K to avoid cooling of gas below that temperature but no upper temperature cutoff for heating.

### 2.3 Turbulent driving

We drive turbulence in a box of size,  $L = 200$  pc with a uniform initial number density of  $1 \text{ cm}^{-3}$  to achieve a velocity dispersion,  $u_{\text{rms}}$ , of  $10 \text{ km s}^{-1}$ . The properties of the turbulent dynamo also depend on the nature of driving: solenoidal (due to processes such as shear and magneto-rotational instability), compressive (due to processes such as supernova explosions, expanding radiation fronts, and spiral shocks), or a mixture of those two (Federrath 2016). We consider two extreme cases for the driving, i.e., either purely solenoidal ( $\nabla \cdot \mathbf{F}_{\text{dri}} = 0$ , referred to as Sol) or purely compressive ( $\nabla \times \mathbf{F}_{\text{dri}} = 0$ , referred to as Comp). We drive the turbulent flow at large scales,  $1 \leq kL/2\pi \leq 3$  ( $k$  being the wavenumber), with a parabolic function of power, which peaks at  $kL/2\pi = 2$  and decreases to zero power at  $kL/2\pi = 1, 3$ . Thus, the turbulent driving scale is approximately equal to  $L/2 \approx 100$  pc. The correlation time of the driving is set to the expected eddy turnover time of the turbulent flow,  $t_0 = (L/2)/u_{\text{rms}} \approx 3.086 \times 10^{14} \text{ s}$  ( $\approx 10 \text{ Myr}$ ).

### 2.4 Explicit diffusion

We have explicit diffusion of velocity (via the term with  $\nu$  in Eq. 2) and magnetic (via the term with  $\eta$  in Eq. 3) fields and these are characterised by the hydrodynamic ( $\text{Re} = u_{\text{rms}}L/(2\nu)$ ) and magnetic ( $\text{Rm} = u_{\text{rms}}L/(2\eta)$ ) Reynolds numbers computed based on the driving scale. We choose  $\nu$  and  $\eta$  such that  $\text{Re} = \text{Rm} = 2000$ .

There will also be numerical diffusion of velocity and magnetic fields due to the discretisation of the grid. For a given number of grid points,  $n_g$ , the Reynolds numbers corresponding to the numerical diffusion is approximately equal to  $2n_g^{4/3}$  (Appendix C in McKee et al. 2020). For our case of  $n_g = 512$ , the numerical Reynolds numbers are roughly equal to 8000. We choose our Reynolds numbers to be 2000 and this ensures that the explicit diffusion is always significantly higher and at larger scales than the numerical diffusion.

### 2.5 Initial conditions

We initialise our simulations with zero velocity, a uniform initial number density of  $1 \text{ cm}^{-3}$ , a uniform initial temperature of 5000 K, and a weak random (zero mean) seed field with root mean square (rms) strength of  $10^{-10} \text{ G}$ . The random seed magnetic field is constructed to follow a power-law magnetic spectrum with a slope of  $3/2$  (Kazantsev 1968). As long as the seed field is weak, the seed field scales or structure would not affect the properties of the turbulent dynamo (Seta & Federrath 2020).

The magnetic field, for both the Sol and Comp cases, grows exponentially (referred to as the kinematic stage) and then reaches a statistically steady state (referred to as the saturated stage) due to the back-reaction of growing magnetic fields on the turbulent flow (e.g., see Fig. 1 in Seta & Federrath 2021a). We run our simulations until the turbulent dynamo achieves the saturated stage ( $t/t_0 = 100$  and 140 for the Sol and Comp cases, respectively). In the next section, we define the phases based on the temperature of the medium and then study the properties of turbulence in the two-phase medium.

## 3 RESULTS: TWO-PHASE MEDIUM

### 3.1 Phase-wise probability distribution functions of density, temperature, and magnetic fields

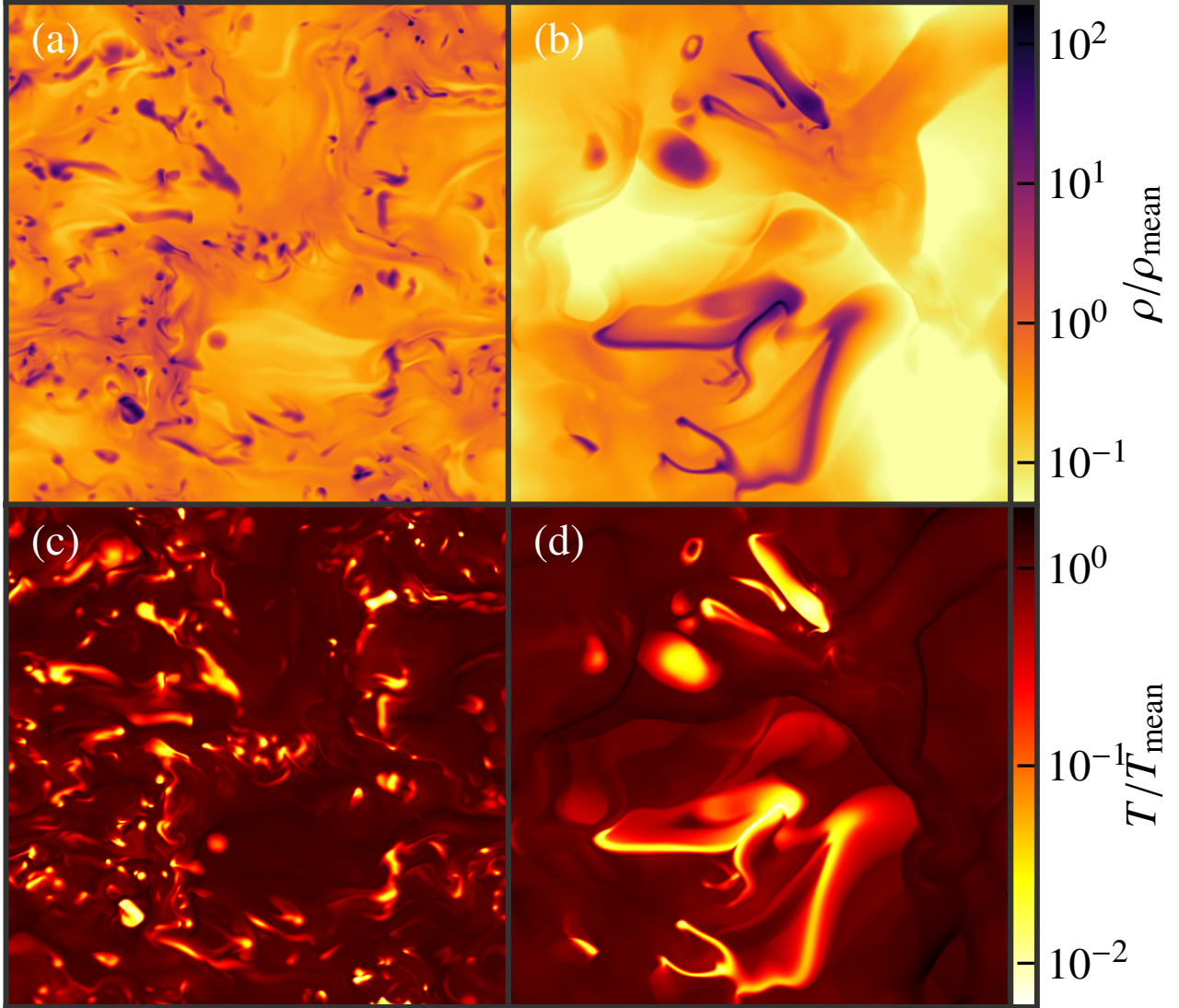
Fig. 1 shows the density and temperature for Sol and Comp runs in the saturated stage of the turbulent dynamo. Both density and temperature vary significantly throughout the domain. On larger scales and especially in the colder regions, structures in the density and temperature seem to be anti-correlated, i.e., regions with higher temperatures have lower densities and vice-versa. The density and temperature structures, especially in the denser and colder regions, for the Sol case are visually smaller in size in comparison to the Comp case. The cold, dense structures are also more numerous for the Sol run. Fig. 2 shows the corresponding velocity and magnetic field structures. On larger scales, the velocity and magnetic structures show some correlation with the density structures but their morphology is complex (compare structures in Fig. 1 (a, b) with Fig. 2 (a, b) and Fig. 2 (c, d)). The magnetic structures seem to exist on scales much larger and smaller than the density structures (for comparison, see Fig. 1 (b) and Fig. 2 in Seta & Federrath 2021b). Thus, the magnetic fields have a complex morphology and do not only depend on the properties of the density of the medium.

In Fig. 3 (a, b), we show the temperature-density diagram (two-dimensional probability distribution function, 2D PDF) for both the Sol and Comp runs in the saturated stage. Both the temperature and density vary over a significant range. The spread towards both the low and high density regions is larger for the Comp case in comparison to the Sol case. In Fig. 3, we also show trends for the following common thermodynamic processes: isothermal ( $T = \text{constant}$ ), isochoric (volume = constant implying  $\rho = \text{constant}$ , as mass is constant in these triply periodic box simulations), isobaric (pressure = constant implying  $\rho T = \text{constant}$ ), and adiabatic ( $T\rho^{1-\gamma_g} = \text{constant}$ , where  $\gamma_g = 5/3$  is the adiabatic index). Parts of the 2D PDF might be comparable to one of these processes but there is always a significant spread. Thus, the temperature-density relationship is complex in these multiphase simulations.

To divide the medium into two phases, for both runs, we choose the temperature cutoff of  $10^3 \text{ K}$ , i.e., gas with  $T < 10^3 \text{ K}$  corresponds to the relatively colder medium and gas with  $T \geq 10^3 \text{ K}$  corresponds to the warm medium. The choice of the temperature cutoff ( $10^3 \text{ K}$ ) is based on its relevance to the ISM (Ferrière 2020). From now on, we divide and study the properties of the medium, turbulence in the medium, and the turbulent dynamo into these two phases. We also always show the properties of the medium as a whole ( $T \geq 0 \text{ K}$ ) for completeness. Now, we revisit the density-temperature relationship phase-wise in Fig. 3. For both cases, the relationship in the  $T < 10^3 \text{ K}$  phase is somewhat closer to the isobaric relationship (in broad agreement with Field et al. 1969; McKee & Ostriker 1977; Cox 2005; Mac Low et al. 2005) but is flatter for the  $T \geq 10^3 \text{ K}$  phase. The upper and lower tails of the distribution tend to be isothermal.

It is important to study and understand the probability distribution function (PDF) of the gas density in the ISM, especially in the cold phase, to construct analytical models of star formation (Federrath & Klessen 2012). In an isothermal setup, the gas density PDF is assumed to follow a lognormal distribution (Vazquez-Semadeni 1994; Passot & Vázquez-Semadeni 1998; Federrath et al. 2008) or a non-lognormal distribution to account for the spatial density intermittency (Hopkins 2013; Squire & Hopkins 2017; Mocz & Burkhardt 2019; Beattie et al. 2021). Even for a non-isothermal gas with a polytropic equation of state, the non-lognormal distribution works well (Federrath & Banerjee 2015). We, here, explore the density PDF in a multiphase medium.



Sol, sat ( $t/t_0 = 100$ )Comp, sat ( $t/t_0 = 140$ )

**Figure 1.** Two-dimensional slices of the normalised density,  $\rho/\rho_{\text{mean}}$ , (a, b) and temperature,  $T/T_{\text{mean}}$ , (c, d) at  $z = L/2$  for Sol (a, c, left-hand panels) and Comp (b, d, right-hand panels) runs in their saturated (sat) stages ( $t/t_0 = 100$  for Sol and  $t/t_0 = 140$  for Comp). Visually, the density and temperature structures are anti-correlated. The cold, dense structures for the Sol case are of smaller sizes but more numerous in comparison to the Comp case.

Fig. 4 show the PDF of densities in the kinematic and saturated stages of the turbulent dynamo for the Sol and Comp cases. For both cases, the PDF for  $T \geq 0$  K region shows a double hump structure re-confirming the two-phase nature of the medium (also agrees with Gazol et al. 2001; Vázquez-Semadeni et al. 2007; Audit & Hennebelle 2010). The PDFs in the kinematic and saturated stages for both cases and all three regions:  $T < 10^3$  K,  $T \geq 10^3$  K, and  $T \geq 0$  K remain roughly the same and thus the growing magnetic field does not have a significant effect on the density distribution.

To each phase for each case, away from the transition region, we fit the PDF of  $s_\rho = \ln(\rho/\rho_{\text{mean}}, T \geq 0 \text{ K})$  to a Gaussian distribution,

$$\mathcal{LN}(s_\rho) = \left(2\pi\sigma_{\mathcal{LN}}^2\right)^{-1/2} \exp\left(-\frac{(s_\rho - s_0)^2}{2\sigma_{\mathcal{LN}}^2}\right), \quad (7)$$

where  $s_0$  and  $\sigma_{\mathcal{LN}}$  are the mean and standard deviation, respectively. The dotted black lines in Fig. 4 show the fitted distribution for each

case. For both the cases, away from the transition region, the lognormal distribution fits the density in the  $T < 10^3$  K and  $T \geq 10^3$  K phases well. This agrees with previous results from supernova-driven turbulence simulations (de Avillez & Breitschwerdt 2004; Mac Low et al. 2005; Gressel 2009; Gent et al. 2013). The density varies over a larger range for the Comp case and the corresponding  $s_0$  and  $\sigma_{\mathcal{LN}}$ , as inferred from the fit, are also higher. Overall, this agrees with the previous results of broader density distributions in case of compressive driving (Federrath et al. 2008).

We show 2D PDFs of magnetic fields and density for both cases in Fig. 5. We also show ideal magnetic field - density relations (dashed black lines) for following types of simple gas compressions (see Fig. 1 in Trites et al. 2015): compression along magnetic field lines ( $b \propto \rho^0$ ), compression perpendicular to magnetic field lines in a cylindrical or filamentary geometry ( $b \propto \rho^{1/2}$ ), spherical compression ( $b \propto \rho^{2/3}$ ), and compression perpendicular to magnetic field

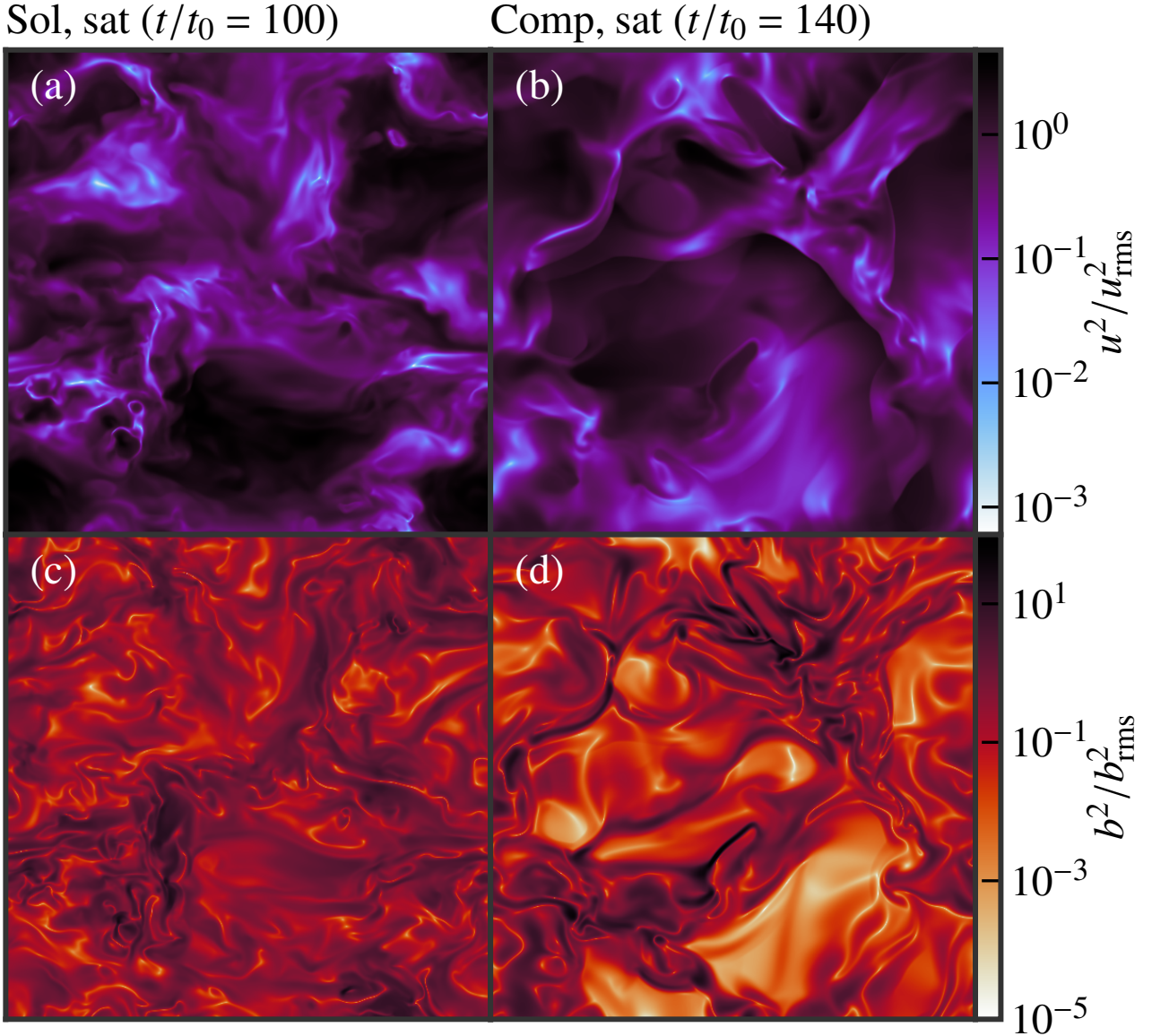


**Figure 2.** Same as Fig. 1 but for the normalised velocity,  $u^2/u_{\text{rms}}^2$ , (a, b) and magnetic fields,  $b^2/b_{\text{rms}}^2$ , (c, d). The velocity and magnetic field structures show some correlation with the density structures shown in Fig. 1 (a, b) but the magnetic structures show a complex morphology, which cannot be directly correlated to the density structures.

lines in a disc-like or slab geometry ( $b \propto \rho^1$ ). The  $b$ - $\rho$  PDF (also see Banerjee et al. 2009) for both the Sol and Comp cases do not agree with those simple trends in these multiphase simulations. Phase-wise, we find that the relationship is roughly similar in all the phases for the Sol run (probably due to significant mixing) but changes with the phase for the Comp case. In the Comp run,  $b$  is more strongly positively correlated with  $\rho$  in the  $T < 10^3$  K phase in comparison to the  $T \geq 10^3$  K phase and this probably implies stronger compressions in the colder regions of the medium. However, there is a significant spread in the data across the fitted trends, which shows a more complex dependence, even in the individual phases. Overall, the correlation analysis implies that the magnetic field strength is not only controlled by the density of the medium.

In Fig. 6, we show the PDF of a single magnetic field component,  $b_x/b_{\text{rms}}$ ,  $T \geq 0$  K in different phases for both the Sol (a) and Comp (b)

cases, respectively. The magnetic field varies over a larger range in the Comp case and this is correlated to the larger range in densities (see Fig. 4). The velocity PDFs in these driven turbulence numerical simulations are Gaussian (see Fig. B1 (c, d) in Appendix B) but the magnetic fields they amplify are highly non-Gaussian or spatially intermittent. This is evident from the heavy tail in the PDF at higher values of  $b_x/b_{\text{rms}}$ ,  $T \geq 0$  K in Fig. 6 and the computed kurtosis much higher than that of a Gaussian distribution (three).

For the Sol case (Fig. 6 (a)), the standard deviation of  $b_x/b_{\text{rms}}$ ,  $T \geq 0$  K for the  $T < 10^3$  K phase in the kinematic stage is higher than that of the  $T \geq 10^3$  K phase by a factor of two (possibly due to stronger compression in the  $T < 10^3$  K phase). On saturation, the standard deviation decreases for the  $T < 10^3$  K phase (effect of the back-reaction of strong magnetic fields) but remains roughly the same for the  $T \geq 10^3$  K phase. The kurtosis is similar in

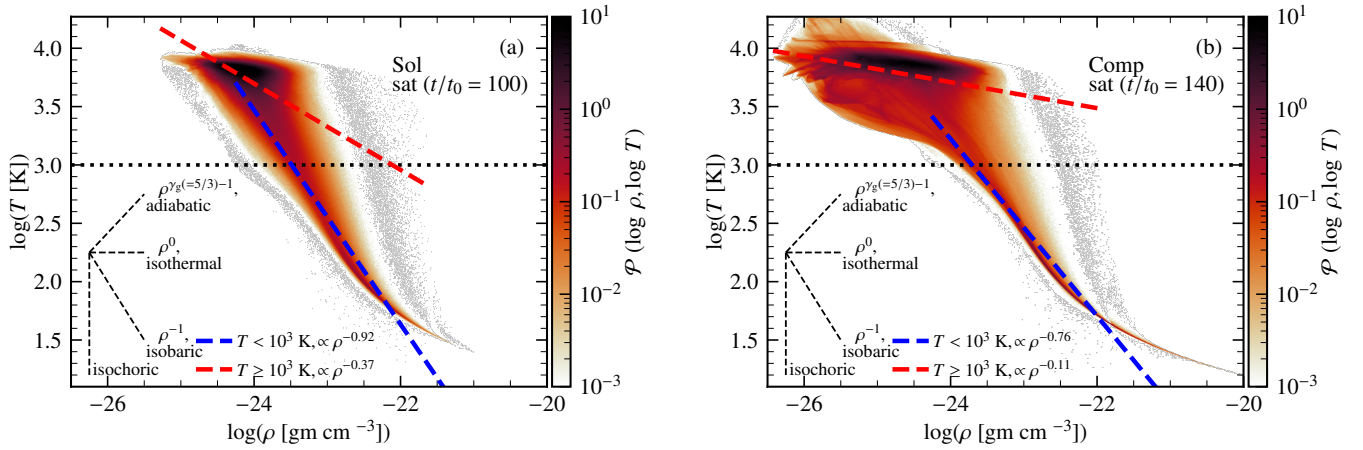


**Figure 3.** Two-dimensional probability distribution functions (2D PDFs) of density and temperature for the Sol (a) and Comp (b) runs with colour showing the corresponding probability,  $\mathcal{P}$ . The dashed black lines show trends for various thermodynamic processes: isochoric ( $\rho = \text{constant}$ ), isobaric ( $\rho T = \text{constant}$ ), isothermal ( $T = \text{constant}$ ), and adiabatic ( $T\rho^{1-\gamma_g} = \text{constant}$ , where  $\gamma_g = 5/3$  is the adiabatic index). For both runs, the  $T - \rho$  relationship in these turbulent, multiphase simulations is complicated and do not follow any of those simple thermodynamic relations. We select  $T = 10^3$  K as the cutoff temperature to distinguish between the phases (dotted black line). Regions with  $T < 10^3$  K represents the relatively colder medium and those with  $T \geq 10^3$  K corresponds to the warm phase. The dashed coloured lines show trends for each phase:  $T < 10^3$  K (blue) and  $T \geq 10^3$  K (red). The trend in the  $T < 10^3$  K phase is closer to the isobaric relation and it flattens in the  $T \geq 10^3$  K phase.

the kinematic stage and also reduces to a similar value on saturation. Thus, the magnetic field intermittency in both the  $T < 10^3$  K and  $T \geq 10^3$  K phases decreases on saturation. This result agrees with the conclusions from the isothermal turbulent dynamo simulations (Schekochihin et al. 2004; Seta et al. 2020; Seta & Federrath 2021a). The kurtosis of the region as a whole ( $T \geq 0$  K) is higher than that of each phase (possibly because of higher contrast in values) but that too decreases on saturation. For the Comp case (Fig. 6 (b)), the standard deviation of  $b_x/b_{\text{rms}}$ ,  $T \geq 0$  K in the kinematic stage is roughly four times higher in the  $T < 10^3$  K phase than that of the  $T \geq 10^3$  K phase (possibly due to an even stronger compression in comparison to the Sol case) and reduces on saturation. Based on the kurtosis, the magnetic field in the  $T \geq 10^3$  K phase is more intermittent than that in the  $T < 10^3$  K phase (also see Appendix C for a characterisation of the tangled state of magnetic field lines in each phase). On saturation, the magnetic intermittency in both the phases decreases but the magnetic field in the  $T \geq 10^3$  K phase of the Comp case still remains more intermittent.

Overall, the densities in each phase (away from the transition region with  $T = 10^3$  K) roughly follow a lognormal distribution and magnetic fields are non-Gaussian (non-Gaussianity decreases as the field saturates). However, each phase is far from being isothermal and there is a dynamic exchange between the phases. The  $T - \rho$  and  $b - \rho$  PDFs are also quite complex and shows signatures of a realistic ISM. In the next subsection, we study the properties of turbulence in the two-phase medium.

### 3.2 Phase-wise properties of the turbulent medium

In Fig. 7, for both Sol and Comp runs, we describe the turbulence in the different phases of the medium via the following three important properties: the volume filling fraction,  $\mathcal{F}$ , rms velocity,  $u_{\text{rms}}$ , and rms Mach number,  $\mathcal{M} = u_{\text{rms}}/c_s$  ( $c_s$  being the sound speed). We show their time evolution over the entire run time.

For the  $T < 10^3$  K phase,  $\mathcal{F}$  is significantly smaller than the  $T \geq 10^3$  K phase (Fig. 7 (a, b)). The colder gas occupies only a very small fraction of the volume (around 3 – 4%) and warmer gas is the primary

volume filling gas (around 97 – 96%). The rms velocity, shown in Fig. 7 (c, d), for both the Sol and Comp cases is very similar for both the phases (it varies significantly over the domain, see Fig. 2 (a, b)) and is approximately equal to  $u_{\text{rms}} \approx 10 \text{ km s}^{-1}$ . This is primarily decided by the turbulent driving (see Sec. 2.3). Finally,  $\mathcal{M}$  is higher in the  $T < 10^3$  K phase ( $\mathcal{M} \approx 5$ ) in comparison to the  $T \geq 10^3$  K phase ( $\mathcal{M} \approx 1$ ) for both the runs ( $\mathcal{M}$  for the  $T < 10^3$  K phase is slightly higher for the Comp run compared to the Sol run). This shows that the  $T < 10^3$  K phase is largely supersonic and the  $T \geq 10^3$  K phase is largely transsonic (locally, the Mach number can vary over a huge range in each phase, see Fig. B2 (c, d) in Appendix B). This is also expected from the observations of the ISM (Gaensler et al. 2011; Schneider et al. 2013; Marchal & Miville-Deschênes 2021). From numerical simulations of the turbulent dynamo in an isothermal gas, the properties of the turbulent dynamo depend on the Mach number of the turbulent flow (Federrath et al. 2011; Seta & Federrath 2021a; Achikanath Chirakkara et al. 2021). In the next section, we explore the properties of the turbulent dynamo in the two-phase medium.

## 4 RESULTS: TURBULENT DYNAMO IN THE TWO-PHASE MEDIUM

Having studied the basic properties of the turbulent two-phase medium, we now focus on the magnetic field amplification by the turbulent dynamo. The goal here is to quantify differences and similarities in dynamo action between different phases of the ISM and also compare these results with those from isothermal turbulent dynamo simulations.

### 4.1 Phase-wise properties of the turbulent dynamo

In Fig. 8, we show the time evolution of the ratio of the magnetic to turbulent kinetic energy,  $E_{\text{mag}}/E_{\text{kin}}$ , for both Sol and Comp runs. The growth rate in the kinematic stage (denoted by  $\gamma$ ) remains approximately the same in both the  $T < 10^3$  K and  $T \geq 10^3$  K phases of the ISM but the saturation level (ratio of  $E_{\text{mag}}/E_{\text{kin}}$  in the saturated



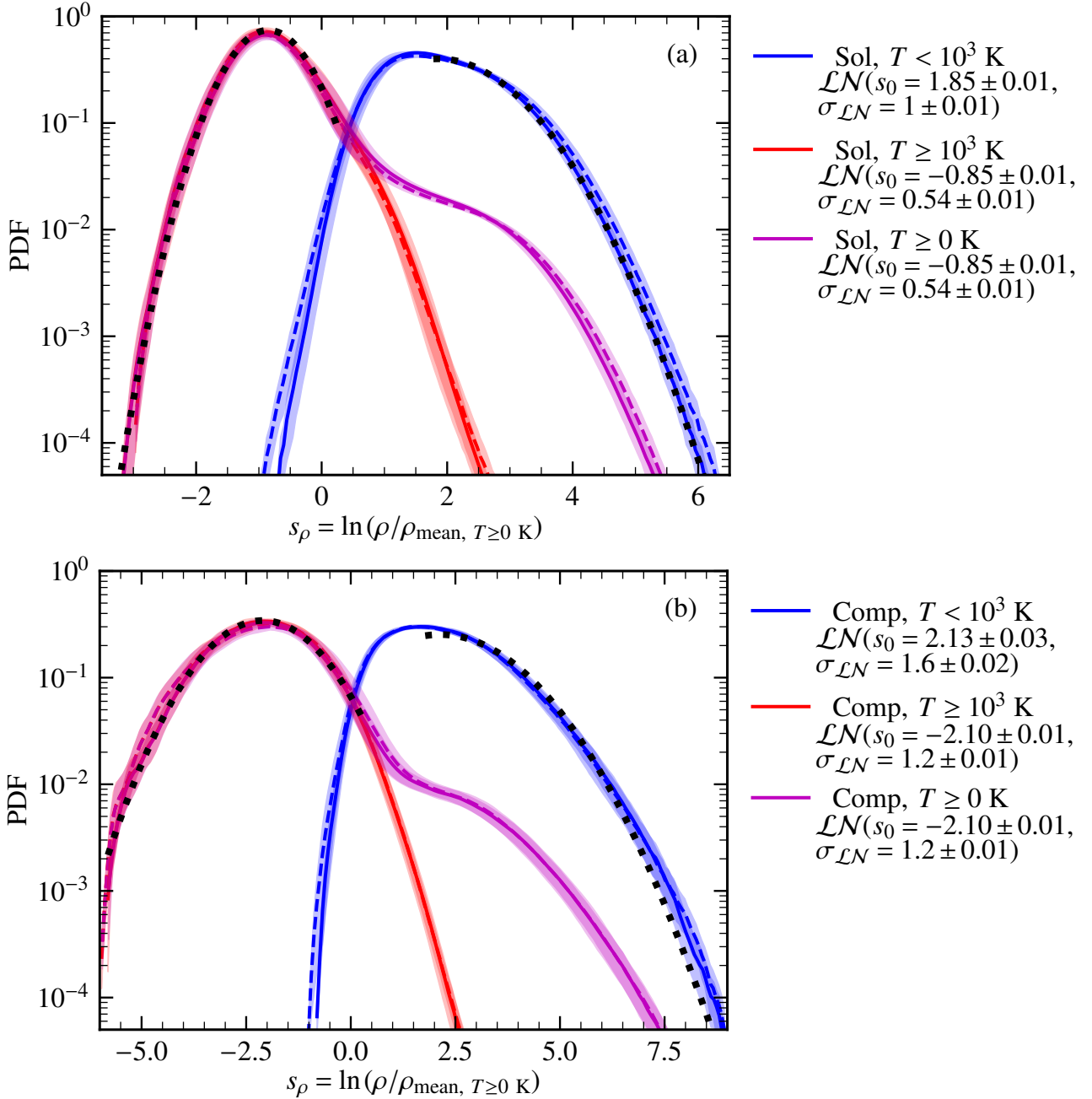


**Figure 4.** PDF of  $s_\rho = \ln(\rho/\rho_{\text{mean}}, T \geq 0 \text{ K})$  in  $T < 10^3$  K (blue),  $T \geq 10^3$  K (red), and  $T \geq 0$  K (magenta) phases for Sol (a) and Comp (b) cases in their respective kinematic (dashed lines) and saturated (solid lines) stages. The shaded region shows one-sigma variation over 20 independent eddy turnover times in each stage. The curves for the kinematic and saturated stages are roughly the same (they lie within the shaded region) and thus the growing magnetic field has almost no effect on the density distribution. The double hump structure for  $T \geq 0$  K region in both cases re-confirms the number of phases to be two. For each phase in each case, away from the transition region (densities around  $T = 10^3$  K), we also fit the distribution of  $s_\rho$  with a Gaussian distribution (Eq. 7, dotted black lines) and the corresponding value of the mean ( $s_0$ ) and standard deviation ( $\sigma_{\mathcal{LN}}$ ) is given in the legend. For both cases, the lognormal distribution fits densities in both the phases well. For the Comp case, the density varies over a larger range and also, from the fit,  $s_0$  and  $\sigma_{\mathcal{LN}}$  are higher.

stage, denoted by  $R_{\text{sat}}$ ) is significantly lower for the  $T < 10^3$  K phase as compared to the  $T \geq 10^3$  K phase. For turbulent dynamo simulations in an isothermal gas at different Mach numbers, the growth rate and saturation level both change with  $\mathcal{M}$  (Federrath et al. 2011; Seta & Federrath 2021a). Considering that the  $T \geq 10^3$  K phase has  $\mathcal{M} \approx 1$  and the  $T < 10^3$  K phase has  $\mathcal{M} \approx 5$ , the growth rate clearly does not agree with the isothermal models but the saturation level

shows the same trend as the isothermal runs (decrease with  $\mathcal{M}$  for  $\mathcal{M} \gtrsim 1$ ).

Federrath et al. (2011) provides an empirical model to compute the growth rate,  $\gamma[t_0^{-1}]$ , and saturation level,  $R_{\text{sat}}$ , as a function of  $\mathcal{M}$  based on the isothermal turbulent dynamo simulations (see their Eq. 3 and Table 1). Using the model, at  $\mathcal{M} = 1$  (comparable to the  $T \geq 10^3$  K medium for our case),  $\gamma \approx 0.78 t_0^{-1}$  for the Sol case and  $\approx 0.30 t_0^{-1}$  for the Comp case. At  $\mathcal{M} = 5$  (comparable to our  $T < 10^3$  K

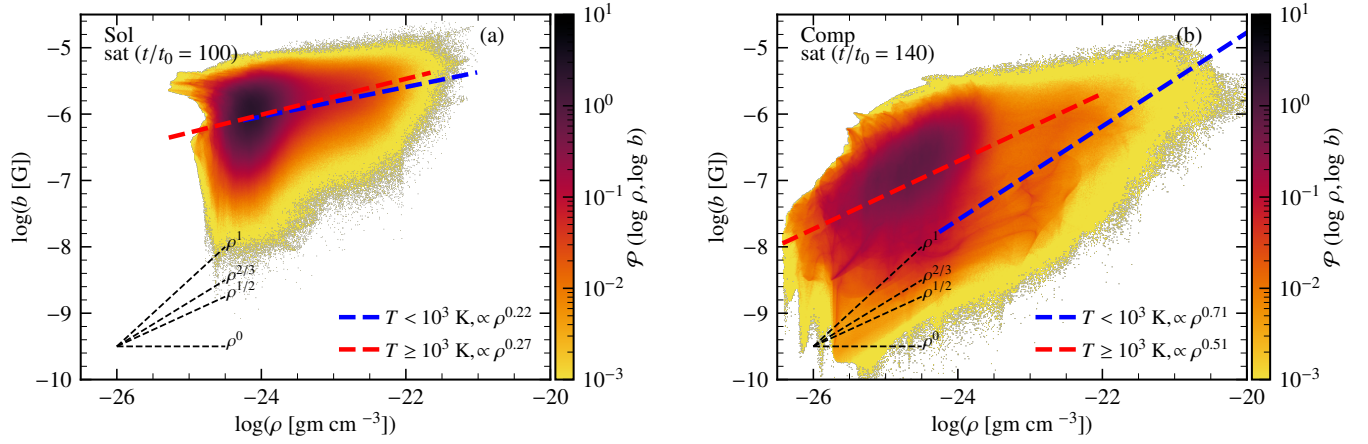


**Figure 5.** Same as Fig. 3 but for 2D PDFs of magnetic field and density. The dashed black lines show  $b$ - $\rho$  relations for simple gas compressions: compression along magnetic field lines ( $\rho^0$ ), compression perpendicular to magnetic field lines ( $b \propto \rho^{1/2}$  for cylindrical/filamentary geometry and  $b \propto \rho^1$  for disc-like/slab geometry), and spherical compression ( $b \propto \rho^{2/3}$ ). The dependence of  $b$  on  $\rho$  in these multi-phase simulations is very complex and cannot be easily described by a single power-law relationship consistent with these simple gas compressions. The dependence of  $b$  on  $\rho$  in these multi-phase simulations is very complex and cannot be easily described by a single power-law relationship consistent with these simple gas compressions. The dependence for the Sol case is very similar in both the phases because of significant mixing. For the Comp case, the  $T < 10^3$  K phase shows a higher slope than the  $T \geq 10^3$  K phase and this points towards significant gas compressions in the colder regions. However, these trends (dashed, blue and red lines) in both the Sol and Comp runs do not fit the data well and there is a significant spread across those lines. This further emphasises a complex dependence and also the fact that the magnetic field does not only depend on the density of the medium.

medium for our case), growth rates from the model are  $\approx 0.53 \tau_0^{-1}$  and  $\approx 0.24 \tau_0^{-1}$  for the Sol and Comp cases, respectively. The growth rate for our runs are same for the  $T < 10^3$  K and  $T \geq 10^3$  K phase in both the Sol ( $\Gamma \approx 0.37 \tau_0^{-1}$ ) and Comp ( $\Gamma \approx 0.18 \tau_0^{-1}$ ) runs and are smaller than corresponding values estimated from the model at both Mach numbers. This shows that overall the turbulent dynamo in non-isothermal gas have smaller growth rates in comparison to its isothermal counterpart. However, the ratio of growth rates for Sol and Comp cases ( $\approx 2$ ) roughly remains the same between the isothermal model and our simulations.

The model suggests that the saturation levels for  $\mathcal{M} = 1$  are  $\approx 0.24$  and  $\approx 0.03$  for the Sol and Comp cases and for  $\mathcal{M} = 5$ , they are  $\approx 0.03$  and  $\approx 0.006$ . We find that for our non-isothermal simulations,  $R_{\text{sat}} \approx 0.13$  and  $\approx 0.019$  for  $T \geq 10^3$  K ( $\mathcal{M} \approx 1$ ) and  $T < 10^3$  K ( $\mathcal{M} \approx 5$ ) phase, respectively, in the Sol run and 0.021 and 0.0024 in the Comp run. We find that  $R_{\text{sat}}$  also is lower than that predicted from the model based on the isothermal turbulent dynamo simulations.

Table 1 summarises the growth rate and saturation level for the turbulent dynamo in isothermal and non-isothermal gases. Both the growth rate and saturation level are lower for the non-isothermal gas for both types of driving. These differences in the growth rate and saturation level with isothermal simulations at appropriate Mach numbers are probably due to significant and continuous energy exchange between the two phases of the medium (Mach number in these multiphase simulations also varies a lot locally, see Fig. B2). This means that the magnetic energy can be passed on between phases and their presence in one phase need not imply they are generated in that phase.

Having studied the phase-wise growth rate and saturation level, in the next subsection, we explore the reason for the roughly equal growth rate in both the phases and the lower saturation level for the  $T < 10^3$  K phase.

## 4.2 Phase-wise vorticity and Lorentz force

The growth of magnetic fields via the turbulent dynamo action is directly connected to vortical motions in the turbulent flow (Mee

& Brandenburg 2006; Federrath et al. 2011) and such motions are quantified by the vorticity,

$$\omega = \nabla \times \mathbf{u}. \quad (8)$$

In fact, the lower growth rate in the case of purely compressive driving in comparison to purely solenoidal driving in isothermal simulations is attributed to the lower vorticity for compressive driving (Federrath et al. 2011). In Fig. 9, we show the rms vorticity,  $\omega_{\text{rms}}$ , for different phases in Sol and Comp runs. First, we too find that  $\omega_{\text{rms}}$  is smaller for the Comp case in comparison to the Sol case. This aligns well with the previous result with regards to the lower growth rate in the case of compressive driving. Next, for both cases in all the phases, the  $\langle \omega_{\text{rms}} \rangle$  (where  $\langle \rangle$  denotes average over time) in the kinematic stage is higher than that in the saturated stage. This is a direct consequence of the back-reaction of strong magnetic fields on the velocity and implies that the amplification of magnetic fields is reduced in the saturated stage. Furthermore, the difference in  $\langle \omega_{\text{rms}} \rangle$  between the kinematic and saturated stage is lower for the Comp case and this is probably because of the smaller saturation level (Fig. 8) and thus weaker back-reaction. However, the amount of vorticity, as measured by  $\omega_{\text{rms}}$ , is approximately equal for both the  $T < 10^3$  K and  $T \geq 10^3$  K phases in both the Sol and Comp runs. This gives rise to an equally efficient dynamo in both the phases and thus probably an equal magnetic field growth rate. We now explicitly study various vorticity generation and destruction terms to explain roughly equal vorticity generation in the  $T < 10^3$  K and  $T \geq 10^3$  K phases of the medium.

The evolution of vorticity is governed by the following equation (Shukurov & Subramanian 2021):

$$\frac{\partial \omega}{\partial t} = \underbrace{\nabla \times (\mathbf{u} \times \omega)}_{\dot{\omega}_{\text{turb}}} + \underbrace{\nu \nabla^2 \omega}_{\dot{\omega}_{\text{diss}}} + \underbrace{\nabla \times \left( \frac{\mathbf{j} \times \mathbf{b}}{c\rho} \right)}_{\dot{\omega}_{\text{Lorentz}}} + \underbrace{\frac{\nabla \rho \times \nabla p_{\text{th}}}{\rho^2}}_{\dot{\omega}_{\text{baroclinic}}} + \underbrace{2\nu \nabla \times (\tau \nabla \ln \rho)}_{\dot{\omega}_{\nabla \ln \rho}} + \underbrace{\nabla \times \mathbf{F}_{\text{dri}}}_{\dot{\omega}_{\text{driv}}}, \quad (9)$$

where  $c$  is the speed of light,  $\mathbf{j} = (c/4\pi) \nabla \times \mathbf{b}$  is the current density, and  $p_{\text{th}}$  is the thermal pressure (other terms are as described after



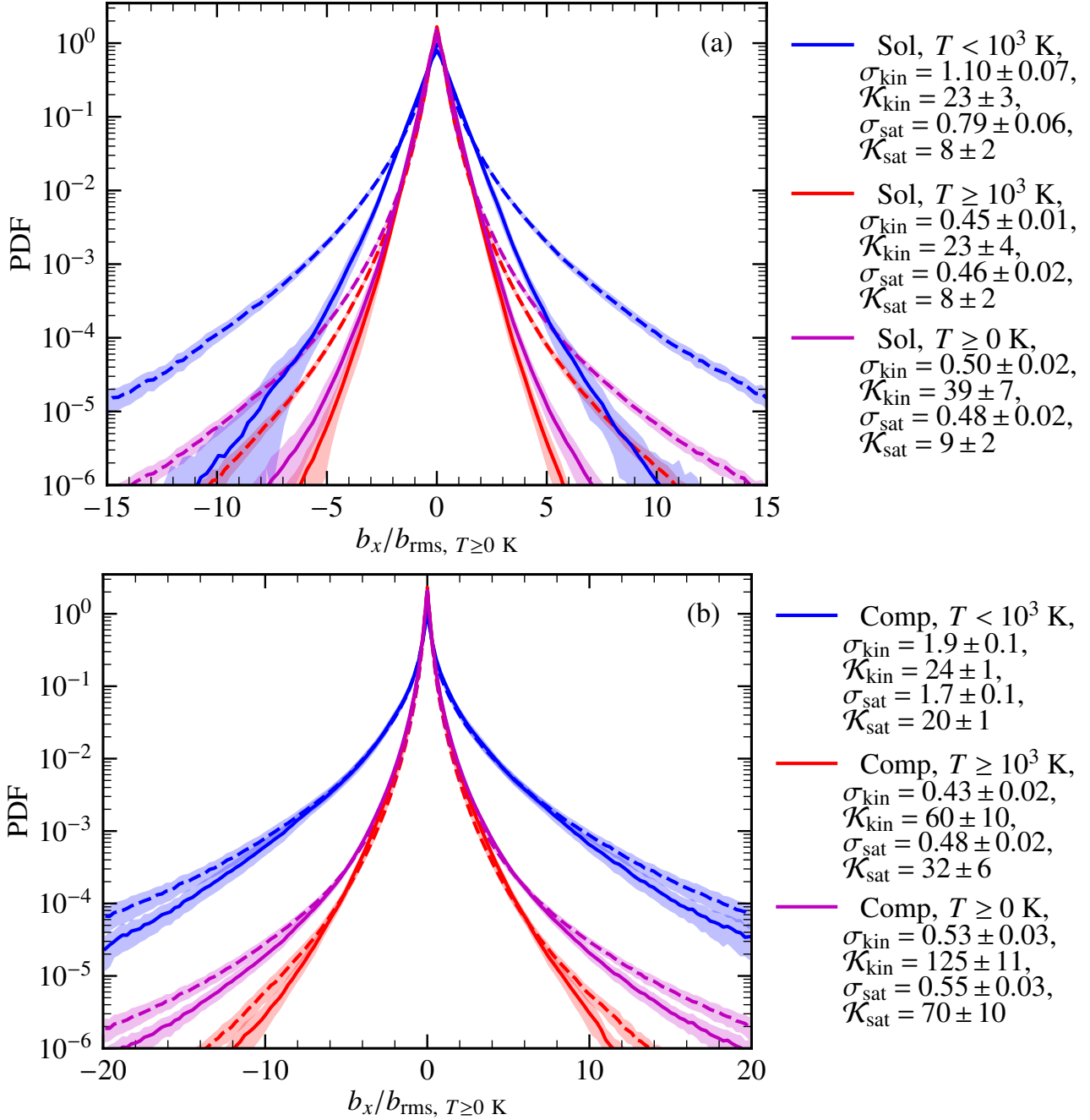


**Figure 6.** Same as Fig. 4 but for the magnetic field component,  $b_x/b_{\text{rms}}, T \geq 0$  K. PDFs are highly non-Gaussian or spatially intermittent and the computed standard deviation ( $\sigma$ ) and kurtosis ( $\mathcal{K}$ ) for the corresponding kinematic (kin) and saturated (sat) stages in each case are given in the legend (the mean and skewness of the distribution  $\approx 0$ ). The standard deviation is always higher for the  $T < 10^3$  K phase as compared to the  $T \geq 10^3$  K phase (roughly by a factor of two for the Sol case and four for the Comp case). On saturation,  $\sigma$  in the  $T < 10^3$  K phase decreases for both cases but in the  $T \geq 10^3$  K phase roughly remains the same. The kurtosis is similar in both the phases for the Sol case but is higher for the  $T \geq 10^3$  K phase in the Comp run. Overall, the kurtosis always decreases on saturation. This implies that the magnetic field in both phases becomes less intermittent as the turbulent dynamo saturates.

Eq. 4). On the right-hand side of Eq. 9, the first term denotes the generation/destruction of vorticity by turbulent motions ( $\dot{\omega}_{\text{turb}}$ , see Batchelor 1950, for a discussion on the analogy between the magnetic induction and vorticity evolution equations), the second term denotes the diffusion of vorticity ( $\dot{\omega}_{\text{diss}}$ ), the third term captures the effect of the Lorentz force ( $\mathbf{j} \times \mathbf{b}/c$ ,  $\dot{\omega}_{\text{Lorentz}}$ ), the fourth term is a baroclinic term ( $\dot{\omega}_{\text{baroclinic}}$ ,  $= 0$  for an isothermal gas), the fifth term is due to viscous interactions in the presence of logarithmic density gradients

( $\dot{\omega}_{\nabla \ln \rho}$ ), and the sixth term is due to the turbulent driving ( $\dot{\omega}_{\text{driv}}$ ,  $= 0$  for purely compressive driving).

Each term in the right-hand side of Eq. 9 is a vector quantity and thus it is difficult to quantify its role in the growth or decay of vorticity. Following Käpylä et al. (2018), we take an inner product of these terms with vorticity and this gives a scalar quantity, the sign of which indicates growth (positive) or decay (negative). Furthermore, we normalise those values by  $\omega_{\text{rms}}$  to preserve the units (e.g.  $\langle \omega \cdot$

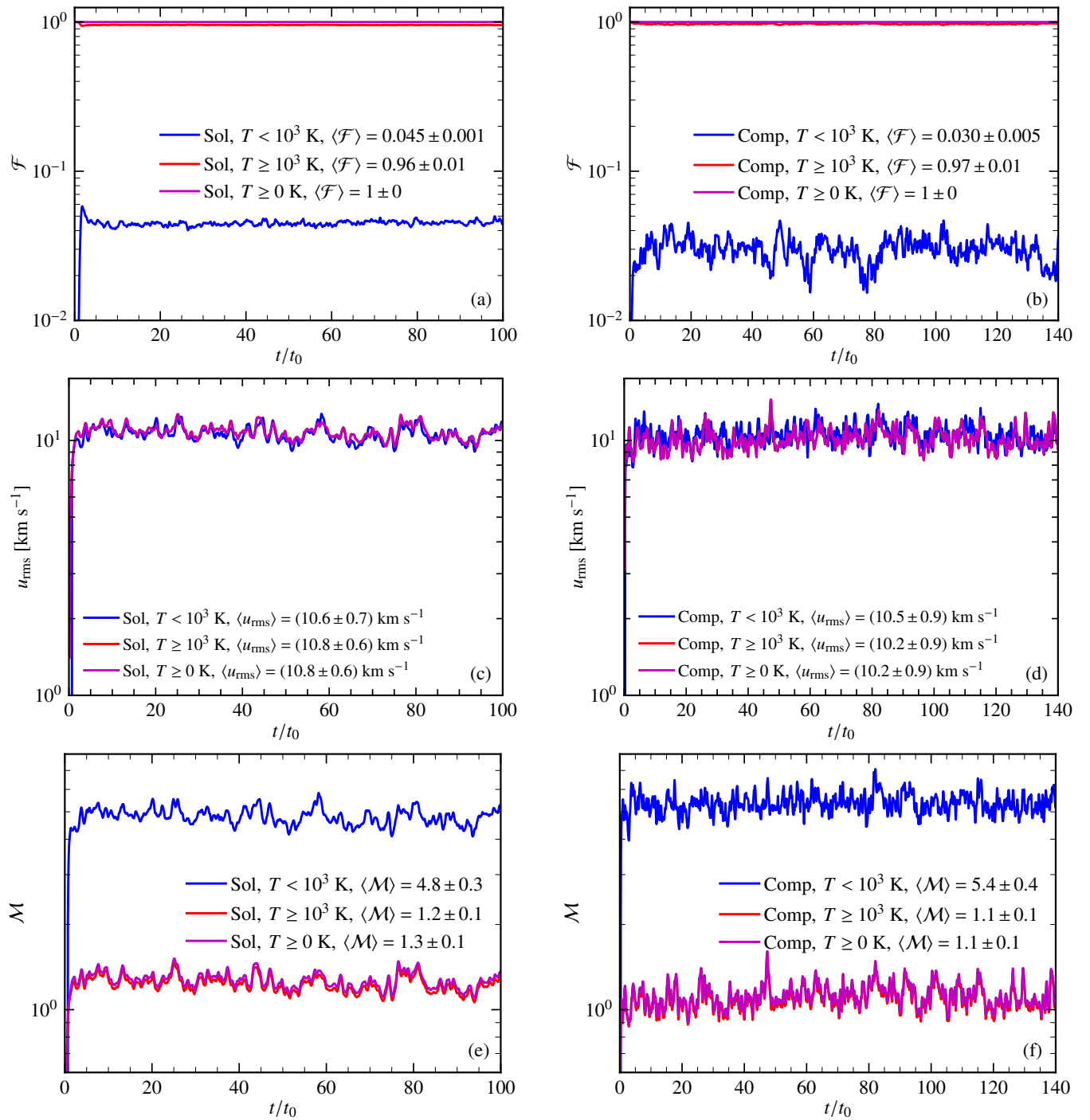


**Figure 7.** Properties of the turbulent medium: volume filling fraction,  $\mathcal{F}$  (a, b), rms velocity,  $u_{\text{rms}}$  (c, d), and rms Mach number,  $\mathcal{M}$  (e, f) as a function of time ( $t/t_0$ ) for the Sol (left-hand panels) and Comp (right-hand panels) runs. They are also divided by the phases:  $T < 10^3$  K (colder, blue),  $T \geq 10^3$  K (warmer, red), and the medium as a whole ( $T \geq 0$  K, magenta). Most of the volume is filled by the warmer  $T \geq 10^3$  K gas and the  $T < 10^3$  K phase occupies only 3–4 % of the volume. For both cases,  $u_{\text{rms}} \approx 10 \text{ km s}^{-1}$ . The  $T < 10^3$  K phase is supersonic ( $\mathcal{M} \approx 5$ ) and the  $T \geq 10^3$  K phase is transsonic ( $\mathcal{M} \approx 1$ ).

$\dot{\omega}_{\text{turb}}/\omega_{\text{rms}}$  has units of  $\text{s}^{-2}$ ). In Fig. 10, we show the time evolution of the mean (over the volume of interest) of these normalised values for the first five terms in the right-hand side of Eq. 9 in different phases for both the Sol and Comp runs. In Table 2, we give their corresponding time averaged values in the kinematic and saturated stages.

For the Sol run, at the start,  $\langle \omega \cdot \dot{\omega}_{\text{driv}} \rangle / \omega_{\text{rms}} \approx 10^{-29} \text{ s}^{-2}$  acts

like a seed term for the vorticity as other terms are negligible. The contribution of this term remains roughly the same throughout the run and is eventually much smaller in comparison to the first five terms. For the Comp run,  $\langle \omega \cdot \dot{\omega}_{\text{driv}} \rangle / \omega_{\text{rms}} \approx 10^{-35} \text{ s}^{-2}$  and is negligible even at the start of the simulation. Here, the dominant terms are  $\langle \omega \cdot \dot{\omega}_{\text{baroclinic}} \rangle / \omega_{\text{rms}}$  and  $\langle \omega \cdot \dot{\omega}_{\nabla \ln \rho} \rangle / \omega_{\text{rms}}$  (both  $\approx 10^{-28} \text{ s}^{-2}$  for  $t/t_0 \lesssim 1$ ). Thus, the initial seed  $\omega$  for the Comp case is primarily

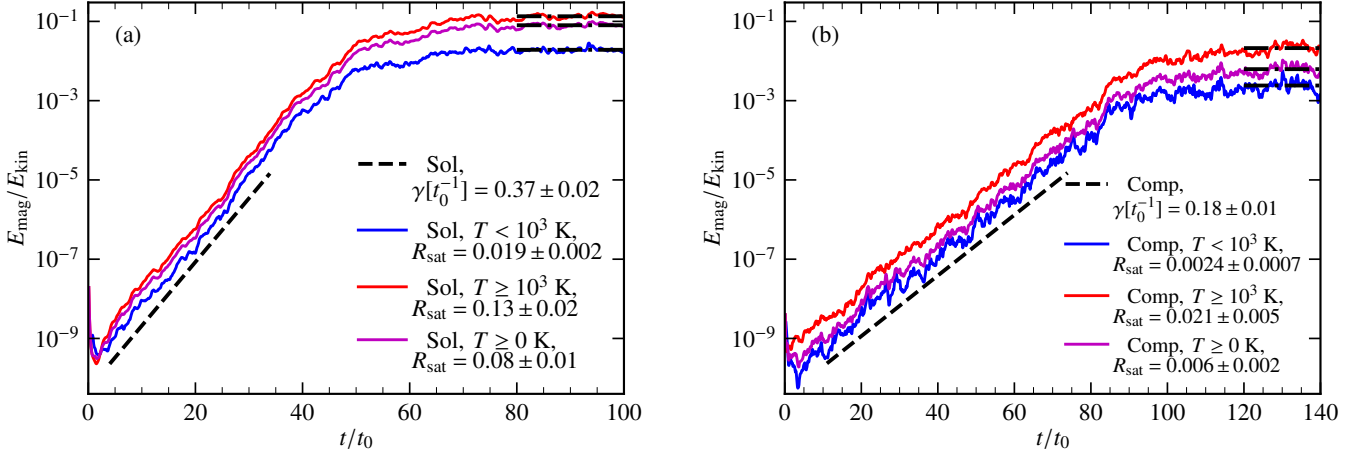


**Figure 8.** Time evolution of  $E_{\text{mag}}/E_{\text{kin}}$  for Sol (a) and Comp (b) runs in different phases of the ISM:  $T < 10^3$  K (blue),  $T \geq 10^3$  K (red), and the medium as a whole ( $T \geq 0$  K, magneta). The dashed line shows the growth rate,  $\gamma[t_0^{-1}]$ , and the dotted-dashed line shows the saturation level,  $R_{\text{sat}}$ . The growth rate is similar for both the phases and the medium as a whole but the saturation level is significantly smaller for the  $T < 10^3$  K phase in comparison to the  $T \geq 10^3$  K phase.

**Table 1.** Table showing the comparison of the growth rate and saturation level between isothermal (using the model in Federrath et al. 2011, at appropriate Mach numbers) and non-isothermal (or multiphase; this work) turbulent dynamo simulations for purely solenoidal (Sol) and purely compressive (Comp) driving. The columns are as follows: 1. nature of driving, 2. phase of the medium, 3. estimated Mach number,  $\mathcal{M}$ , 4. growth rate in the non-isothermal case,  $\gamma[t_0^{-1}]$ , 5. growth rate in the isothermal case at the appropriate Mach number,  $\gamma_{\text{iso}}[t_0^{-1}]$ , 6. relative difference in the growth rate between the isothermal and non-isothermal cases,  $\Delta\gamma/\gamma = (\gamma_{\text{iso}} - \gamma)/\gamma$ , 7. saturation level in the non-isothermal case,  $R_{\text{sat}}$ , 8. saturation level in the isothermal case at the appropriate Mach number,  $R_{\text{sat,iso}}$ , and 9. relative difference in the saturation level between the isothermal and non-isothermal cases,  $\Delta R_{\text{sat}}/R_{\text{sat}} = (R_{\text{sat,iso}} - R_{\text{sat}})/R_{\text{sat}}$ .

Driving	Phase	$\mathcal{M}$	$\gamma[t_0^{-1}]$	$\gamma_{\text{iso}}[t_0^{-1}]$	$\Delta\gamma/\gamma$	$R_{\text{sat}}$	$R_{\text{sat,iso}}$	$\Delta R_{\text{sat}}/R_{\text{sat}}$
Sol	$T < 10^3$ K	$4.8 \pm 0.3$	$0.37 \pm 0.02$	0.53	0.43	$0.019 \pm 0.002$	0.03	0.58
	$T \geq 10^3$ K	$1.2 \pm 0.1$	$0.37 \pm 0.02$	0.78	1.11	$0.13 \pm 0.02$	0.24	0.85
Comp	$T < 10^3$ K	$5.4 \pm 0.4$	$0.18 \pm 0.01$	0.24	0.33	$0.0024 \pm 0.0007$	0.006	1.50
	$T \geq 10^3$ K	$1.1 \pm 0.1$	$0.18 \pm 0.01$	0.30	0.66	$0.021 \pm 0.005$	0.03	0.43

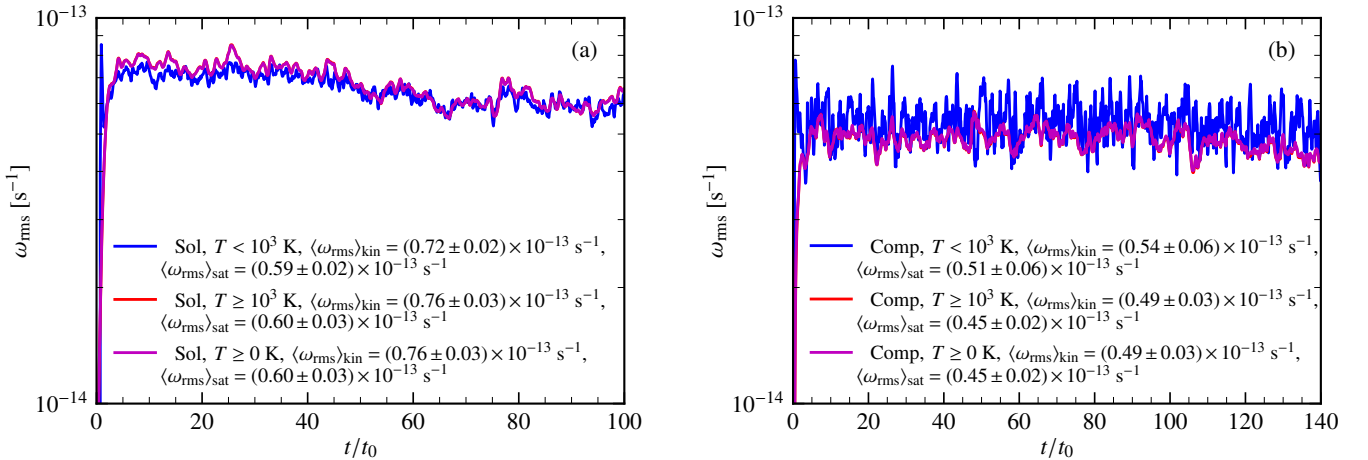


**Figure 9.** Time evolution of the rms vorticity,  $\omega_{\text{rms}}$ , for different phases ( $T < 10^3$  K,  $T \geq 10^3$  K, and  $T \geq 0$  K) in Sol (a) and Comp (b) runs. In the legend, we also give the  $\omega_{\text{rms}}$  averaged over the kinematic ( $t/t_0 = 5$  to  $35$  for the Sol run and  $t/t_0 = 12$  to  $75$  for the Comp run) and saturated ( $t/t_0 = 80$  to  $100$  for the Sol run and  $t/t_0 = 120$  to  $140$  for the Comp run) stages.  $\omega_{\text{rms}}$  is always smaller for the Comp run making it a less efficient dynamo. Also,  $\langle \omega_{\text{rms}} \rangle_{\text{kin}} > \langle \omega_{\text{rms}} \rangle_{\text{sat}}$  for both cases and thus the growth of magnetic fields is reduced as the dynamo saturates. Finally,  $\omega_{\text{rms}}$  is roughly similar between both the  $T < 10^3$  K and  $T \geq 10^3$  K phases for both runs in their respective kinematic and saturated stages. This is the probably reason for the approximately equal growth rate in different phases of the medium, as seen in Fig. 8.



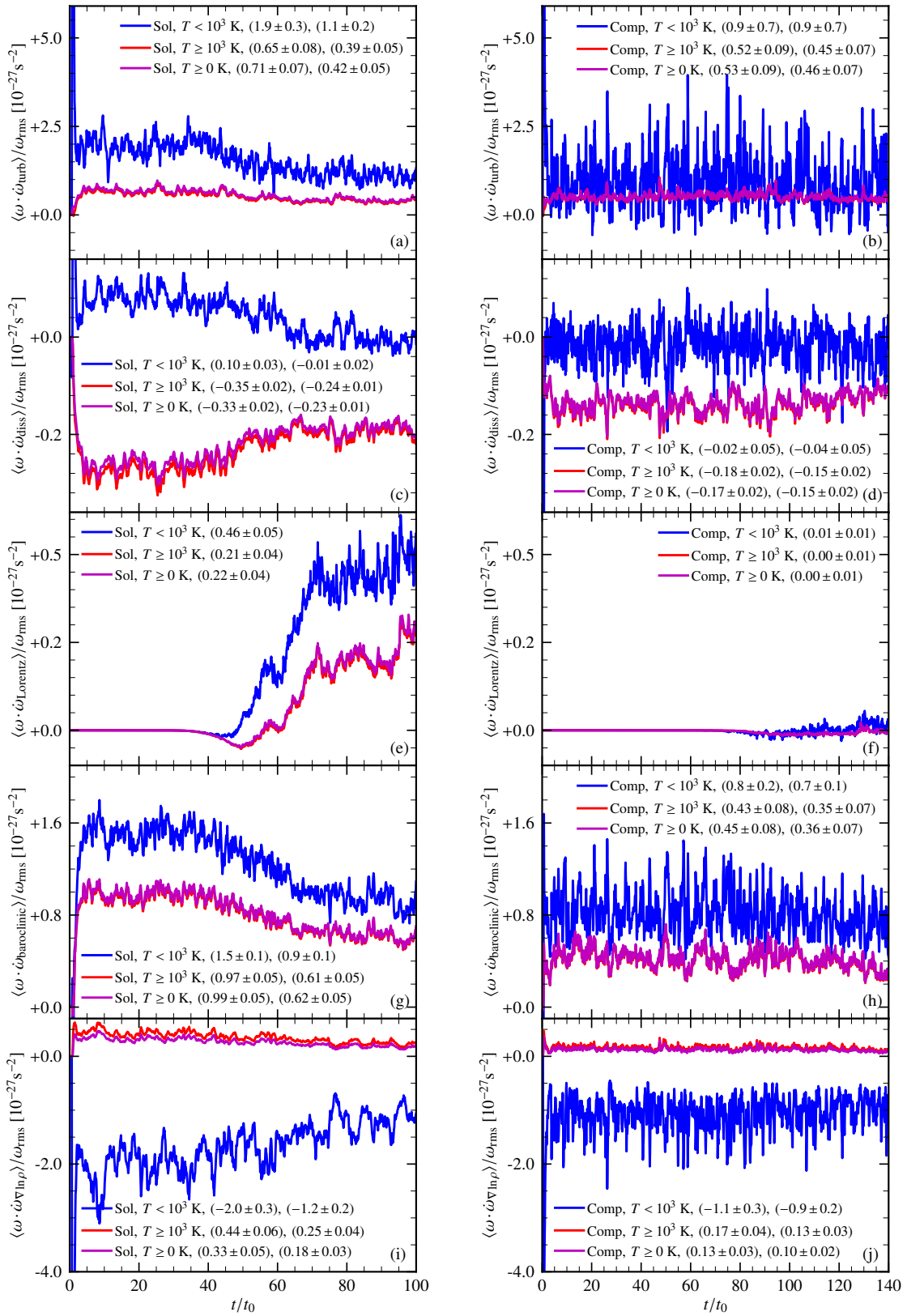


**Figure 10.** Volume average of inner product of first five terms on the right-hand side of the vorticity ( $\omega$ ) evolution equation (Eq. 9) with  $\omega$ , normalised by the  $\omega_{\text{rms}}$ , for the Sol and Comp runs in all three phases:  $T < 10^3$  K (blue),  $T \geq 10^3$  K (red), and  $T \geq 0$  K (magenta). The corresponding time averaged values in the kinematic and saturated stages are given in the legend. Initially, for the Sol run,  $\omega$  seed is from  $\dot{\omega}_{\text{driv}}$  ( $\langle \omega \cdot \dot{\omega}_{\text{driv}} \rangle / \omega_{\text{rms}} \approx 10^{-29} \text{ s}^{-2}$ ) and for the Comp case, it is from  $\dot{\omega}_{\text{baroclinic}}$  and  $\dot{\omega}_{\nabla \ln \rho}$  (for  $t/t_0 \leq 1$ ,  $\langle \omega \cdot \dot{\omega}_{\text{baroclinic}} \rangle / \omega_{\text{rms}} \approx \langle \omega \cdot \dot{\omega}_{\nabla \ln \rho} \rangle / \omega_{\text{rms}} \approx 10^{-28} \text{ s}^{-2}$ ). For both runs,  $\dot{\omega}_{\text{turb}}$  is always dominant and positive (implying vorticity amplification) in all phases. Additionally, for the  $T < 10^3$  K phase,  $\dot{\omega}_{\nabla \ln \rho}$  is dominant (negative, implying vorticity destruction) and for the  $T \geq 10^3$  K phase,  $\dot{\omega}_{\text{baroclinic}}$  (positive, implying vorticity amplification) is dominant. These dominant terms for each case decreases as the magnetic field saturates.  $\dot{\omega}_{\text{diss}}$  and  $\dot{\omega}_{\text{Lorentz}}$  are always sub-dominant.

**Table 2.** Summary of volume averaged inner products of vorticity generation/destruction terms with vorticity, normalised by  $\omega_{\text{rms}}$ , and then time averaged in their respective kinematic and saturated stages for both types of driving (Fig. 10). The columns are as follows: 1. nature of driving, 2. phase, 3. stage, kin: kinematic and sat: saturated, 4. turbulent amplification/decay term,  $\dot{\omega}_{\text{turb}}$ , 5. viscous dissipation term,  $\dot{\omega}_{\text{diss}}$ , 6. Lorentz force term,  $\dot{\omega}_{\text{Lorentz}}$ , 7. baroclinic term,  $\dot{\omega}_{\text{baroclinic}}$ , 8. viscous interactions due to logarithmic density gradients,  $\dot{\omega}_{\nabla \ln \rho}$ , and 9. dominant terms out of all five terms. Columns 4 – 8 are in units of  $10^{-27} \text{s}^{-2}$ .

Driving	Phase	Stage	$\langle \omega \cdot \dot{\omega}_{\text{turb}} \rangle / \omega_{\text{rms}}$	$\langle \omega \cdot \dot{\omega}_{\text{diss}} \rangle / \omega_{\text{rms}}$	$\langle \omega \cdot \dot{\omega}_{\text{Lorentz}} \rangle / \omega_{\text{rms}}$	$\langle \omega \cdot \dot{\omega}_{\text{baroclinic}} \rangle / \omega_{\text{rms}}$	$\langle \omega \cdot \dot{\omega}_{\nabla \ln \rho} \rangle / \omega_{\text{rms}}$	Dominant terms
	$T < 10^3 \text{ K}$	kin	$1.9 \pm 0.3$	$0.10 \pm 0.03$	--	$1.5 \pm 0.1$	$-2.0 \pm 0.3$	$\dot{\omega}_{\text{turb}}, \dot{\omega}_{\nabla \ln \rho}$
		sat	$1.1 \pm 0.2$	$-0.01 \pm 0.02$	$0.46 \pm 0.05$	$0.9 \pm 0.1$	$-1.2 \pm 0.2$	$\dot{\omega}_{\text{turb}}, \dot{\omega}_{\nabla \ln \rho}$
Sol	$T \geq 10^3 \text{ K}$	kin	$0.65 \pm 0.08$	$-0.35 \pm 0.02$	--	$0.97 \pm 0.05$	$0.44 \pm 0.06$	$\dot{\omega}_{\text{baroclinic}}, \dot{\omega}_{\text{turb}}$
		sat	$0.39 \pm 0.05$	$-0.24 \pm 0.01$	$0.21 \pm 0.04$	$0.61 \pm 0.05$	$0.25 \pm 0.04$	$\dot{\omega}_{\text{baroclinic}}, \dot{\omega}_{\text{turb}}$
	$T \geq 0 \text{ K}$	kin	$0.71 \pm 0.07$	$-0.33 \pm 0.02$	--	$0.99 \pm 0.05$	$0.33 \pm 0.05$	$\dot{\omega}_{\text{baroclinic}}, \dot{\omega}_{\text{turb}}$
		sat	$0.42 \pm 0.05$	$-0.23 \pm 0.01$	$0.22 \pm 0.04$	$0.62 \pm 0.05$	$0.18 \pm 0.03$	$\dot{\omega}_{\text{baroclinic}}, \dot{\omega}_{\text{turb}}$
	$T < 10^3 \text{ K}$	kin	$0.9 \pm 0.7$	$-0.02 \pm 0.05$	--	$0.8 \pm 0.2$	$-1.1 \pm 0.3$	$\dot{\omega}_{\text{turb}}, \dot{\omega}_{\nabla \ln \rho}$
		sat	$0.9 \pm 0.7$	$-0.04 \pm 0.05$	$0.01 \pm 0.01$	$0.7 \pm 0.1$	$-0.9 \pm 0.2$	$\dot{\omega}_{\text{turb}}, \dot{\omega}_{\nabla \ln \rho}$
Comp	$T \geq 10^3 \text{ K}$	kin	$0.52 \pm 0.09$	$-0.18 \pm 0.02$	--	$0.43 \pm 0.08$	$0.17 \pm 0.04$	$\dot{\omega}_{\text{turb}}, \dot{\omega}_{\text{baroclinic}}$
		sat	$0.52 \pm 0.09$	$-0.15 \pm 0.02$	$0.00 \pm 0.01$	$0.35 \pm 0.07$	$0.13 \pm 0.03$	$\dot{\omega}_{\text{turb}}, \dot{\omega}_{\text{baroclinic}}$
	$T \geq 0 \text{ K}$	kin	$0.53 \pm 0.09$	$-0.17 \pm 0.02$	--	$0.45 \pm 0.08$	$0.13 \pm 0.03$	$\dot{\omega}_{\text{turb}}, \dot{\omega}_{\text{baroclinic}}$
		sat	$0.46 \pm 0.07$	$-0.15 \pm 0.02$	$0.00 \pm 0.01$	$0.36 \pm 0.07$	$0.10 \pm 0.02$	$\dot{\omega}_{\text{turb}}, \dot{\omega}_{\text{baroclinic}}$

generated by the fourth ( $\dot{\omega}_{\text{baroclinic}}$ ) and fifth ( $\dot{\omega}_{\nabla \ln \rho}$ ) terms in these multiphase simulations.

In the kinematic stage of the turbulent dynamo, as expected, the effect of Lorentz force ( $\dot{\omega}_{\text{Lorentz}}$ , see Fig. 10 (e, f)) is negligible and thus the vorticity is primarily controlled by the other four terms, which are  $\dot{\omega}_{\text{turb}}$ ,  $\dot{\omega}_{\text{diss}}$ ,  $\dot{\omega}_{\text{baroclinic}}$ , and  $\dot{\omega}_{\nabla \ln \rho}$ . All these four terms are significant in strength but  $\dot{\omega}_{\text{turb}}$  is always one of the dominant terms for both the phases in the Sol and Comp runs (see the last column in Table 2) and it is positive, which implies vorticity amplification.  $\dot{\omega}_{\text{baroclinic}}$  is equally strong (and positive, so amplifying vorticity) in the  $T \geq 10^3 \text{ K}$  phase (in fact slightly more than  $\dot{\omega}_{\text{turb}}$  for the Sol run) but is weaker for the  $T < 10^3 \text{ K}$  phase, primarily because of compression which aligns density and pressure gradients. On the other hand,  $\dot{\omega}_{\nabla \ln \rho}$  is weaker in the  $T \geq 10^3 \text{ K}$  phase and stronger (though negative, so destroying vorticity) in  $T < 10^3 \text{ K}$  phase because of higher density and density gradients in the colder regions of the medium. These relative trends are similar for the Sol and Comp cases but the fluctuations are larger in the Comp case, probably indicating these terms act on a larger length scales (also, see a larger size of density or temperature structures in Fig. 1 for the Comp case in comparison to the Sol case). The smaller size of density structures in the Sol case might also lead to more misaligned density and pressure gradients, which in turn would enhance the baroclinic term (as also seen in Fig. 10 and Eq. 9). Overall, these terms combined give a similar level of  $\omega_{\text{rms}}$  in both the phases of the medium, which in turn probably gives a roughly equal growth rate of the turbulent dynamo.

As the magnetic field saturates,  $\dot{\omega}_{\text{Lorentz}}$  increases but still remains sub-dominant compared to the other terms in all the phases for both the Sol and Comp runs. In the saturated stage, the value for the dominant terms for all cases decreases in comparison to the kinematic stage. This leads to a lower  $\omega_{\text{rms}}$  in Fig. 9, which in turn leads to a reduction in the growth of magnetic fields (also see Seta & Federrath 2021a, for a similar conclusion via other probes). The viscous dissipation term,  $\dot{\omega}_{\text{diss}}$ , is always small compared to the other terms for all cases and this is probably because of a well resolved

physical velocity diffusion (see Sec. 2.4). For the Comp run, the net effect of these terms is weaker (implying a weaker growth rate) compared to the Sol case and they also have a smaller difference between the kinematic and saturated stages (implying a weaker back-reaction).

In summary,  $\dot{\omega}_{\text{turb}}$  (see the next paragraph for further discussion on this term) is always dominant and positive in both the phases. In the  $T < 10^3 \text{ K}$  phase, the  $\dot{\omega}_{\nabla \ln \rho}$  term is strong (negative, destruction of vorticity) and in the  $T \geq 10^3 \text{ K}$  phase, the  $\dot{\omega}_{\text{baroclinic}}$  term is strong (positive, amplification of vorticity). The other terms are quite sub-dominant in comparison to these terms. These trends remain the same for both the stages and types of driving (see Table 2).

The turbulent amplification/destruction term in the vorticity evolution equation ( $\dot{\omega}_{\text{turb}}$  in Eq. 9) can be further expanded into

$$\underbrace{\nabla \times (\mathbf{u} \times \boldsymbol{\omega})}_{\dot{\omega}_{\text{turb}}} = \underbrace{(\boldsymbol{\omega} \cdot \nabla) \mathbf{u}}_{\dot{\omega}_{\text{str}}} - \underbrace{(\mathbf{u} \cdot \nabla) \boldsymbol{\omega}}_{\dot{\omega}_{\text{adv}}} - \underbrace{\boldsymbol{\omega} (\nabla \cdot \mathbf{u})}_{\dot{\omega}_{\text{com}}}, \quad (10)$$

where the first term denotes amplification of vorticity by stretching ( $\dot{\omega}_{\text{str}}$ ), the second term denotes advection of vorticity ( $\dot{\omega}_{\text{adv}}$ ), and the third term denotes compression of vorticity ( $\dot{\omega}_{\text{com}}$ , this can lead to amplification or destruction of vorticity depending on the local compression or expansion). Like with each term in Eq. 9, we take an inner product of these terms with  $\boldsymbol{\omega}$  and normalise it by  $\omega_{\text{rms}}$ . The time evolution of the mean (over the volume of interest) of these quantities is shown in Fig. 11 and their time averaged values in the kinematic and saturated stages are given in Table 3.

The vortex stretching term,  $\dot{\omega}_{\text{str}}$ , is dominant in the  $T \geq 10^3 \text{ K}$  phase (also, in the  $T \geq 0 \text{ K}$  phase or the entire region) and the vortex compression term,  $\dot{\omega}_{\text{com}}$ , is dominant in the  $T < 10^3 \text{ K}$  phase (though it is negative, implying growth of vorticity, see Table 3). Thus,  $\dot{\omega}_{\text{turb}}$  always leads to amplification of vorticity though via different physical processes, vortex compression in the  $T < 10^3 \text{ K}$  phase and vortex stretching in the  $T \geq 10^3 \text{ K}$  phase. In the Comp case,  $\dot{\omega}_{\text{adv}}$  is also high and positive, implying significant local advection of vorticity by

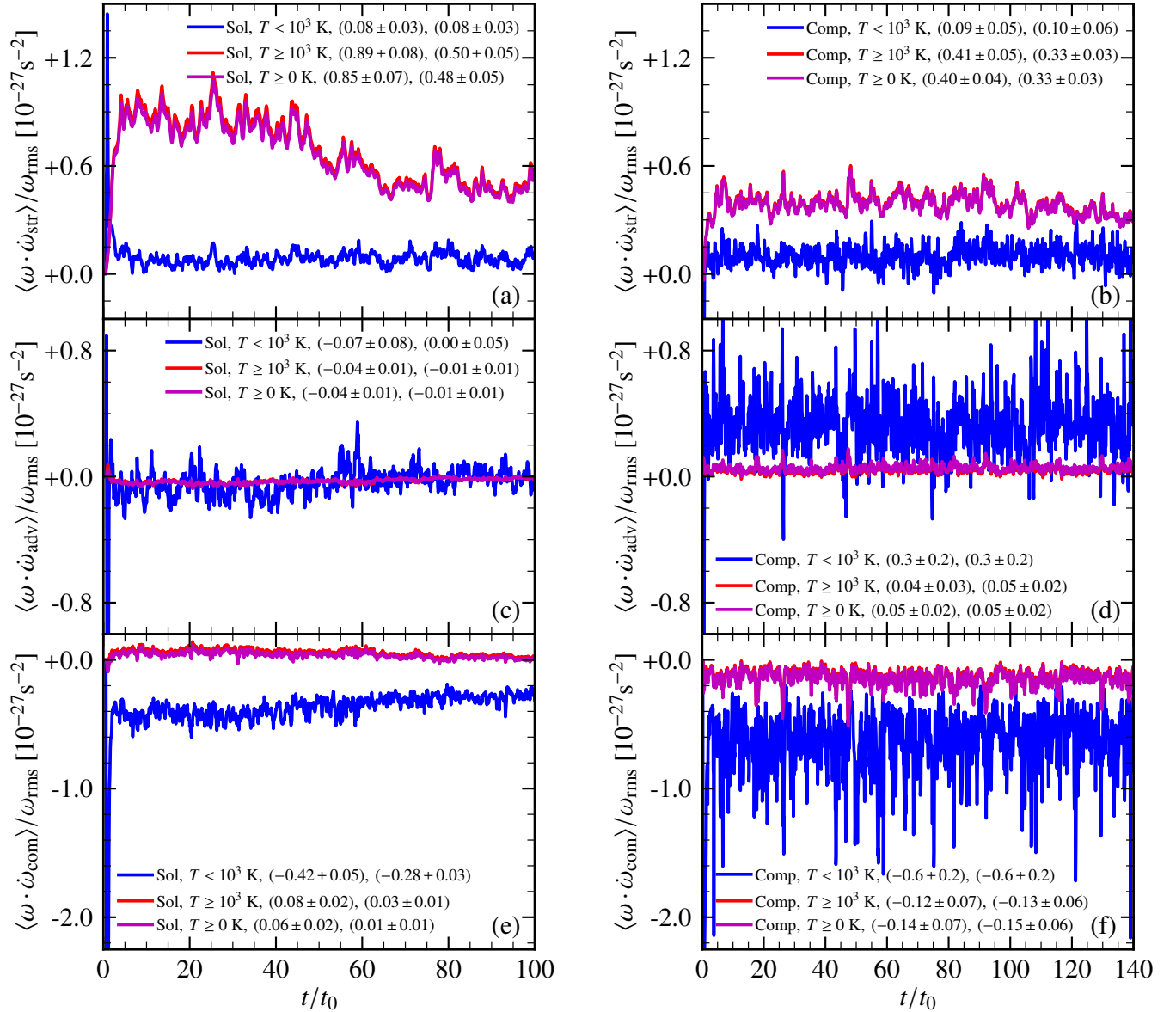


**Figure 11.** Same as Fig. 10 but for  $\dot{\omega}_{\text{str}}$ ,  $\dot{\omega}_{\text{adv}}$ , and  $\dot{\omega}_{\text{com}}$  (Eq. 10). In the  $T < 10^3$  K phase,  $\dot{\omega}_{\text{com}}$  is dominant (though negative, so leads to vorticity amplification) and in the  $T \geq 10^3$  K phase,  $\dot{\omega}_{\text{str}}$  is dominant.  $\dot{\omega}_{\text{adv}}$  is always very sub-dominant except in the  $T < 10^3$  K phase for the Comp run.

turbulent motions. This also leads to an overall reduction in vorticity in comparison to the Sol case.

After exploring the reason for a similar growth rate between the phases, we now study the reason for the lower saturation level for the  $T < 10^3$  K phase as compared to the  $T \geq 10^3$  K phase (see Fig. 8). Fig. 12 shows the rms strength of the Lorentz force,  $|\mathbf{j} \times \mathbf{b}/c|_{\text{rms}}$ , in both the phases and the medium as a whole ( $T \geq 0$  K) for the Sol and Comp runs. The Lorentz force and thus the back-reaction is stronger in the  $T < 10^3$  K phase as compared to the  $T \geq 10^3$  K phase for both types of driving (this also indicates a difference in local magnetic field structure between the phases, see Appendix C for further discussion). Thus, the magnetic fields in the  $T < 10^3$  K phase stop growing slightly earlier than the  $T \geq 10^3$  K phase due to a stronger Lorentz force and this leads to a lower saturation level (note that the growth rate is the same for both phases). The trends are similar for both the Sol and Comp runs.

## 5 SUMMARY AND CONCLUSIONS

With a motivation to explore magnetic fields in different phases of the ISM, we use driven turbulence numerical simulations with prescribed (Milky Way type) heating and cooling function (Sec. 2.2) to study the turbulent dynamo action in a non-isothermal gas (most previous work studies the turbulent dynamo in an isothermal setting). Our main aim is to understand how the properties of the turbulent dynamo and the magnetic field it amplifies depend on the phase of the medium.

We numerically solve the equations of non-ideal compressible magnetohydrodynamics (Eq. 1 – Eq. 4) for a monatomic, ideal gas in a box of size 200 pc and turbulence being continually driven with a root mean square (rms) velocity of  $10 \text{ km s}^{-1}$ . We use two extreme cases for the driving: purely solenoidal (Sol) and purely compressive (Comp). Initially, the simulation is setup with a uniform number



**Table 3.** Same as Table 2 but for vortex stretching ( $\dot{\omega}_{\text{str}}$ , column 4), advection ( $\dot{\omega}_{\text{adv}}$ , column 5), and compression ( $\dot{\omega}_{\text{com}}$ , column 6). Columns 4 – 6 are in units of  $10^{-27} \text{ s}^{-2}$  (Fig. 11) and the last column shows the dominant terms out of all three terms.

Driving	Phase	Stage	$\langle \omega \cdot \dot{\omega}_{\text{str}} \rangle / \omega_{\text{rms}}$	$\langle \omega \cdot \dot{\omega}_{\text{adv}} \rangle / \omega_{\text{rms}}$	$\langle \omega \cdot \dot{\omega}_{\text{com}} \rangle / \omega_{\text{rms}}$	Dominant terms
Sol	$T < 10^3 \text{ K}$	kin	$0.08 \pm 0.03$	$-0.07 \pm 0.08$	$-0.42 \pm 0.05$	$\dot{\omega}_{\text{com}}$
		sat	$0.08 \pm 0.03$	$0.00 \pm 0.05$	$-0.28 \pm 0.03$	$\dot{\omega}_{\text{com}}$
	$T \geq 10^3 \text{ K}$	kin	$0.89 \pm 0.08$	$-0.04 \pm 0.01$	$0.08 \pm 0.02$	$\dot{\omega}_{\text{str}}$
		sat	$0.50 \pm 0.05$	$-0.01 \pm 0.01$	$0.03 \pm 0.01$	$\dot{\omega}_{\text{str}}$
	$T \geq 0 \text{ K}$	kin	$0.85 \pm 0.07$	$-0.04 \pm 0.01$	$0.06 \pm 0.02$	$\dot{\omega}_{\text{str}}$
		sat	$0.48 \pm 0.05$	$-0.01 \pm 0.01$	$0.01 \pm 0.01$	$\dot{\omega}_{\text{str}}$
Comp	$T < 10^3 \text{ K}$	kin	$0.09 \pm 0.05$	$0.3 \pm 0.2$	$-0.6 \pm 0.2$	$\dot{\omega}_{\text{com}}, \dot{\omega}_{\text{adv}}$
		sat	$0.10 \pm 0.06$	$0.3 \pm 0.2$	$-0.6 \pm 0.2$	$\dot{\omega}_{\text{com}}, \dot{\omega}_{\text{adv}}$
	$T \geq 10^3 \text{ K}$	kin	$0.41 \pm 0.05$	$0.04 \pm 0.03$	$-0.12 \pm 0.07$	$\dot{\omega}_{\text{str}}$
		sat	$0.33 \pm 0.03$	$0.05 \pm 0.02$	$-0.13 \pm 0.06$	$\dot{\omega}_{\text{str}}$
	$T \geq 0 \text{ K}$	kin	$0.40 \pm 0.04$	$0.05 \pm 0.02$	$-0.14 \pm 0.07$	$\dot{\omega}_{\text{str}}$
		sat	$0.33 \pm 0.03$	$0.05 \pm 0.02$	$-0.15 \pm 0.06$	$\dot{\omega}_{\text{str}}$

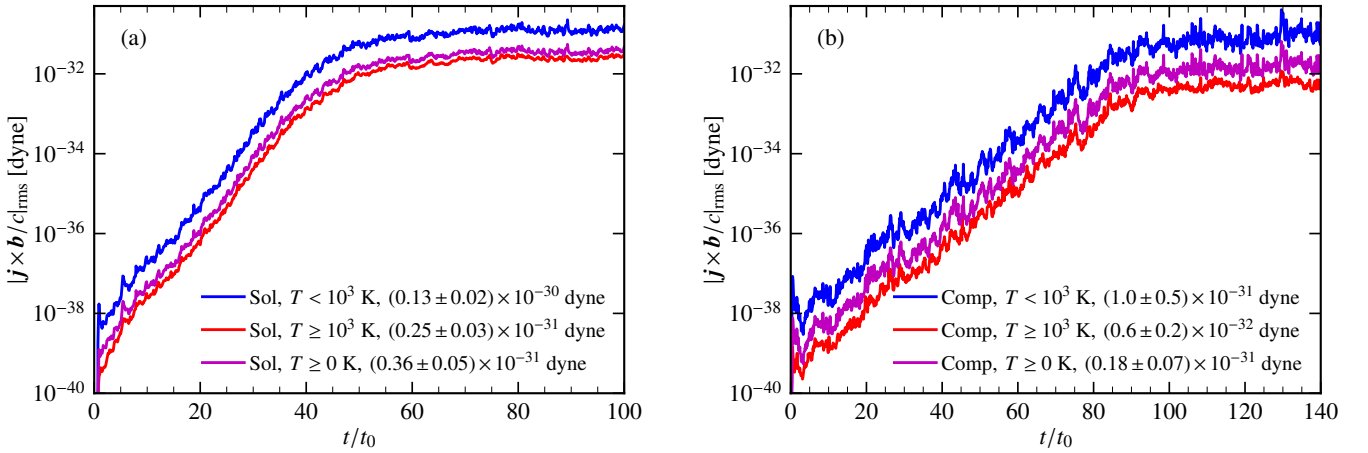


**Figure 12.** RMS strength of the Lorentz force,  $|\mathbf{j} \times \mathbf{b}/c|_{\text{rms}}$ , in different phases for both the Sol (a) and Comp (b) runs. For both cases, the Lorentz force is stronger in the  $T < 10^3 \text{ K}$  phase as compared to the  $T \geq 10^3 \text{ K}$  phase. This leads to a stronger back-reaction and thus a lower saturation level for the  $T < 10^3 \text{ K}$  phase.

density of  $1 \text{ cm}^{-3}$ , a uniform temperature of  $5000 \text{ K}$ , and a weak random seed field with rms strength of  $10^{-10} \text{ G}$ .

As expected, the magnetic field amplifies exponentially and then saturates due to the back-reaction by strong magnetic fields on the turbulent flow. We chose a cutoff temperature of  $10^3 \text{ K}$  for phase division, i.e.,  $T < 10^3 \text{ K}$  phase for the cold medium and  $T \geq 10^3 \text{ K}$  phase for the warm medium (Fig. 1). We then study the properties of turbulence and magnetic fields separately in these two phases. The key results and conclusions from the study are summarised below:

- The 2D PDFs of temperature-density and magnetic field-density are complex and do not follow simple trends (Fig. 3 and Fig. 5). The density PDF roughly follows a lognormal distribution in both the  $T < 10^3 \text{ K}$  and  $T \geq 10^3 \text{ K}$  phases (Fig. 4). The magnetic field is non-Gaussian in both the phases and the non-Gaussianity decreases on saturation (Fig. 6).

- Each phase individually is far from an isothermal gas and there is a continuous dynamic energy exchange between the phases.

- For both the Sol and Comp driving, the  $T < 10^3 \text{ K}$  phase occupies a very small fraction of the volume ( $\lesssim 4\%$ ) and is highly supersonic ( $\mathcal{M} \approx 5$ ). On the other hand, the  $T \geq 10^3 \text{ K}$  phase fills a large fraction of the volume ( $\gtrsim 96\%$ ) and is transsonic ( $\mathcal{M} \approx 1$ ).

- The magnetic field growth rate in the exponential growth phase (kinematic stage) is the same for both the phases ( $T < 10^3 \text{ K}$  and  $T \geq 10^3 \text{ K}$ , Fig. 8). This disagrees with isothermal turbulent dynamo runs at different Mach numbers, where the growth rate decreases with  $\mathcal{M}$  for  $\mathcal{M} \gtrsim 1$ . Once the turbulent dynamo saturates, the ratio of the magnetic to turbulent kinetic energy (saturation level) is lower for the  $T < 10^3 \text{ K}$  phase and this result aligns with isothermal turbulent dynamo simulations. The growth rate and saturation level for the Sol driving is higher than the Comp driving and thus, also in agreement with isothermal runs, the Sol driving gives a more efficient turbulent dynamo. However, for both the Sol and Comp cases, the growth rate

and saturation level in our non-isothermal simulations are lower than the respective isothermal turbulent dynamo runs at appropriate Mach numbers (Table 1). This suggests that the turbulent dynamo action in a non-isothermal gas is different from its isothermal counterpart and this difference is probably due to continuous energy (including the magnetic energy) exchange between the two phases.

- We show that the growth rate is the same in different phases because an approximately equal rms vorticity is generated in both the phases (Fig. 9). Furthermore, the vorticity in the Comp run is lower than that in the Sol run, leading to a less efficient turbulent dynamo. The rms vorticity also decreases on saturation, which implies a weaker amplification of magnetic fields. This is a direct consequence of the back-reaction of strong magnetic fields on the turbulent flow.

- We study different terms responsible for the growth and destruction of vorticity (Eq. 9, Fig. 10, and Table 2). The turbulent amplification/destruction term ( $\dot{\omega}_{\text{turb}}$ ) is always a dominant (always positive, implying vorticity amplification) term for all cases. In addition, the baroclinic term ( $\dot{\omega}_{\text{baroclinic}}$ ) is dominant and positive (implying vorticity amplification) in the  $T \geq 10^3$  K phase (due to misaligned density and pressure gradients) and the term for viscous interactions in the presence of logarithmic density gradients ( $\dot{\omega}_{\nabla \ln \rho}$ ) is dominant and negative (implying vorticity destruction) in the cold phase (due to higher density and density gradients). The viscous dissipation ( $\dot{\omega}_{\text{diss}}$ ) and Lorentz force ( $\dot{\omega}_{\text{Lorentz}}$ ) terms are always sub-dominant. Overall, the combination of these terms gives equal rms vorticity in both the phases of the medium.

- We further study the contribution of vortex stretching ( $\dot{\omega}_{\text{str}}$ ), advection ( $\dot{\omega}_{\text{adv}}$ ), and compression ( $\dot{\omega}_{\text{com}}$ ) to  $\dot{\omega}_{\text{turb}}$  (Eq. 10, Fig. 11, and Table 3).  $\dot{\omega}_{\text{str}}$  is strongest in the  $T \geq 10^3$  K phase and  $\dot{\omega}_{\text{com}}$  (though negative, so amplifying vorticity) is strongest in the  $T < 10^3$  K phase.  $\dot{\omega}_{\text{adv}}$  is quite low except in the  $T < 10^3$  K phase of the Comp case.

- The magnetic field grows at an equal rate in both the phases (as suggested by the equal growth rate) but the growth first stops in the colder phase due to a stronger Lorentz force (Fig. 12).

In the future, we plan to explore the following two extensions of the present work. First, we aim to study the power spectrum of velocity and magnetic fields in different phases. However, this has to be done via structure functions (Mohapatra et al. 2022a; Seta et al. 2022) as each phase is randomly distributed in space, which leads to a non-uniform separation and thus it would be difficult to compute the power spectrum directly. Second, we aim to simulate the multiphase medium generated by supernova-driven turbulence. This would also have the hot ( $\sim 10^6$  K) gas and then the turbulent dynamo can be studied separately in all the three phases (cold, warm, and hot) of the multiphase ISM.

## ACKNOWLEDGEMENTS

We thank the anonymous referee for their useful comments and suggestions. C. F. acknowledges funding provided by the Australian Research Council (Future Fellowship FT180100495), and the Australia-Germany Joint Research Cooperation Scheme (UA-DAAD). We further acknowledge high-performance computing resources provided by the Leibniz Rechenzentrum and the Gauss Centre for Supercomputing (grants pr32lo, pn73fi, and GCS Large-scale project 22542), and the Australian National Computational Infrastructure (grant ek9) in the framework of the National Computational Merit Allocation Scheme and the ANU Merit Allocation Scheme.

## DATA AVAILABILITY

The data from simulations is available upon a reasonable request to the corresponding author, Amit Seta ([amit.seta@anu.edu.au](mailto:amit.seta@anu.edu.au)).

## REFERENCES

- Achikanath Chirakkara R., Federrath C., Trivedi P., Banerjee R., 2021, *Phys. Rev. Lett.*, **126**, 091103
- Audit E., Hennebelle P., 2010, *Astron. Astrophys.*, **511**, A76
- Banerjee R., Vázquez-Semadeni E., Hennebelle P., Klessen R. S., 2009, *Mon. Not. R. Astron. Soc.*, **398**, 1082
- Batchelor G. K., 1950, *Proceedings of the Royal Society of London Series A*, **201**, 405
- Beattie J. R., Mocz P., Federrath C., Klessen R. S., 2021, arXiv e-prints, p. [arXiv:2109.10470](https://arxiv.org/abs/2109.10470)
- Beattie J. R., Krumholz M. R., Federrath C., Sampson M., Crocker R. M., 2022, arXiv e-prints, p. [arXiv:2203.13952](https://arxiv.org/abs/2203.13952)
- Beck R., 2016, *Ann. Rev. Astron. Astrophys.*, **24**, 4
- Beck R., Brandenburg A., Moss D., Shukurov A., Sokoloff D., 1996, *Ann. Rev. Astron. Astrophys.*, **34**, 155
- Beck R., Chamandy L., Elson E., Blackman E. G., 2019, *Galaxies*, **8**, 4
- Borlaff A. S., et al., 2021, *Astrophys. J.*, **921**, 128
- Boulares A., Cox D. P., 1990, *Astrophys. J.*, **365**, 544
- Brandenburg A., Subramanian K., 2005, *Phys. Rep.*, **417**, 1
- Campbell J. L., et al., 2021, arXiv e-prints, p. [arXiv:2112.03247](https://arxiv.org/abs/2112.03247)
- Cesarsky C. J., 1980, *Ann. Rev. Astron. Astrophys.*, **18**, 289
- Cesarsky C. J., Kulsrud R. M., 1981, in Setti G., Spada G., Wolfendale A. W., eds, IAU Symposium Vol. 94, Origin of Cosmic Rays. p. 251
- Cox D. P., 2005, *Ann. Rev. Astron. Astrophys.*, **43**, 337
- de Avillez M. A., Breitschwerdt D., 2004, *Astron. Astrophys.*, **425**, 899
- Dubey A., et al., 2008, Challenges of Extreme Computing using the FLASH code. p. 145
- Elmegreen B. G., 2009, in Andersen J., Nordströara m B., Bland-Hawthorn J., eds, Vol. 254, The Galaxy Disk in Cosmological Context. pp 289–300 ([arXiv:0810.5406](https://arxiv.org/abs/0810.5406)), doi:10.1017/S1743921308027713
- Elmegreen B. G., Scalo J., 2004, *Ann. Rev. Astron. Astrophys.*, **42**, 111
- Farber R., Ruszkowski M., Yang H. Y. K., Zweibel E. G., 2018, *Astrophys. J.*, **856**, 112
- Federrath C., 2015, *Mon. Not. R. Astron. Soc.*, **450**, 4035
- Federrath C., 2016, *Journal of Plasma Physics*, **82**, 535820601
- Federrath C., Banerjee S., 2015, *Mon. Not. R. Astron. Soc.*, **448**, 3297
- Federrath C., Klessen R. S., 2012, *Astrophys. J.*, **761**, 156
- Federrath C., Klessen R. S., Schmidt W., 2008, *Astrophys. J. Lett.*, **688**, L79
- Federrath C., Chabrier G., Schober J., Banerjee R., Klessen R. S., Schleicher D. R. G., 2011, *Phys. Rev. Lett.*, **107**, 114504
- Federrath C., Schober J., Bovino S., Schleicher D. R. G., 2014, *Astrophys. J.*, **797**, L19
- Federrath C., et al., 2017, in Crocker R. M., Longmore S. N., Bicknell G. V., eds, IAU Symposium Vol. 322, The Multi-Messenger Astrophysics of the Galactic Centre. pp 123–128 ([arXiv:1609.08726](https://arxiv.org/abs/1609.08726)), doi:10.1017/S1743921316012357
- Federrath C., Klessen R. S., Iapichino L., Beattie J. R., 2021, *Nature Astronomy*, **5**, 365
- Ferrière K., 2020, *Plasma Physics and Controlled Fusion*, **62**, 014014
- Field G. B., Goldsmith D. W., Habing H. J., 1969, *Astrophys. J. Lett.*, **155**, L149
- Fletcher A., Beck R., Shukurov A., Berkhuijsen E. M., Horellou C., 2011, *Mon. Not. R. Astron. Soc.*, **412**, 2396
- Fryxell B., et al., 2000, *ApJS*, **131**, 273
- Gaensler B. M., et al., 2011, *Nature*, **478**, 214
- Gazol A., Vázquez-Semadeni E., Sánchez-Salcedo F. J., Scalo J., 2001, *Astrophys. J. Lett.*, **557**, L121
- Gent F. A., Shukurov A., Fletcher A., Sarson G. R., Mantere M. J., 2013, *Mon. Not. R. Astron. Soc.*, **432**, 1396
- Gent F. A., Mac Low M.-M., Käpylä M. J., Singh N. K., 2021, *Astrophys. J. Lett.*, **910**, L15

- Gressel O. L., 2009, PhD thesis, University of Potsdam, Germany
- Haugen N. E., Brandenburg A., Dobler W., 2004, *Phys. Rev. E*, **70**, 016308
- Haverkorn M., 2015, in Lazarian A., de Gouveia Dal Pino E. M., Melioli C., eds, *Astrophysics and Space Science Library Vol. 407, Magnetic Fields in Diffuse Media*. p. 483 (arXiv:1406.0283), doi:10.1007/978-3-662-44625-6\_17
- Heiles C., Troland T. H., 2005, *Astrophys. J.*, **624**, 773
- Hopkins P. F., 2013, *Mon. Not. R. Astron. Soc.*, **430**, 1880
- Käpylä M. J., Gent F. A., Väisälä M. S., Sarson G. R., 2018, *Astron. Astrophys.*, **611**, A15
- Kazantsev A. P., 1968, *Soviet Journal of Experimental and Theoretical Physics*, **26**, 1031
- Koyama H., Inutsuka S.-i., 2000, *Astrophys. J.*, **532**, 980
- Koyama H., Inutsuka S.-i., 2002, *Astrophys. J. Lett.*, **564**, L97
- Krause F., Rädler K. H., 1980, Mean-field magnetohydrodynamics and dynamo theory
- Krumholz M. R., Burkhardt B., Forbes J. C., Crocker R. M., 2018, *Mon. Not. R. Astron. Soc.*, **477**, 2716
- Kulsrud R. M., Anderson S. W., 1992, *Astrophys. J.*, **396**, 606
- Mac Low M.-M., Klessen R. S., 2004, *Reviews of Modern Physics*, **76**, 125
- Mac Low M.-M., Balsara D. S., Kim J., de Avillez M. A., 2005, *Astrophys. J.*, **626**, 864
- Mandal A., Federrath C., Körtgen B., 2020, *Mon. Not. R. Astron. Soc.*, **493**, 3098
- Marchal A., Miville-Deschênes M.-A., 2021, *Astrophys. J.*, **908**, 186
- McKee C. F., Ostriker J. P., 1977, *Astrophys. J.*, **218**, 148
- McKee C. F., Stacy A., Li P. S., 2020, *Mon. Not. R. Astron. Soc.*, **496**, 5528
- Mee A. J., Brandenburg A., 2006, *Mon. Not. R. Astron. Soc.*, **370**, 415
- Mocz P., Burkhardt B., 2019, *Astrophys. J. Lett.*, **884**, L35
- Mohapatra R., Jetti M., Sharma P., Federrath C., 2022a, *Mon. Not. R. Astron. Soc.*, **510**, 2327
- Mohapatra R., Jetti M., Sharma P., Federrath C., 2022b, *Mon. Not. R. Astron. Soc.*, **510**, 3778
- Ogbo D. C. S., Green J. A., Dawson J. R., Breen S. L., Mao S. A., McClure-Griffiths N. M., Robshaw T., Harvey-Smith L., 2020, *Mon. Not. R. Astron. Soc.*, **493**, 199
- Pakmor R., Springel V., 2013, *Mon. Not. R. Astron. Soc.*, **432**, 176
- Passot T., Vázquez-Semadeni E., 1998, *Phys. Rev. E*, **58**, 4501
- Raymond J. C., 1992, *Astrophys. J.*, **384**, 502
- Rincon F., 2019, *Journal of Plasma Physics*, **85**, 205850401
- Ruzmaikin A. A., Sokoloff D. D., Shukurov A. M., eds, 1988, *Magnetic fields of galaxies Astrophysics and Space Science Library Vol. 133*, doi:10.1007/978-94-009-2835-0.
- Scalo J., Elmegreen B. G., 2004, *Ann. Rev. Astron. Astrophys.*, **42**, 275
- Schekochihin A. A., Cowley S. C., Taylor S. F., Maron J. L., McWilliams J. C., 2004, *Astrophys. J.*, **612**, 276
- Schneider N., et al., 2013, *Astrophys. J. Lett.*, **766**, L17
- Seta A., Federrath C., 2020, *Mon. Not. R. Astron. Soc.*, **499**, 2076
- Seta A., Federrath C., 2021a, *Physical Review Fluids*, **6**, 103701
- Seta A., Federrath C., 2021b, *Mon. Not. R. Astron. Soc.*, **502**, 2220
- Seta A., Bushby P. J., Shukurov A., Wood T. S., 2020, *Phys. Rev. Fluids*, **5**, 043702
- Seta A., Federrath C., Livingston J. D., McClure-Griffiths N. M., 2022, *Mon. Not. R. Astron. Soc.*, submitted
- Shetty R., Ostriker E. C., 2006, *Astrophys. J.*, **647**, 997
- Shukurov A., Sokoloff D., 2008, in Cardin P., Cugliandolo L., eds, *Les Houches*, Vol. 88, *Dynamos*. Elsevier, pp 251 – 299
- Shukurov A., Subramanian K., 2021, *Astrophysical Magnetic Fields: From Galaxies to the Early Universe*. Cambridge Astrophysics, Cambridge University Press
- Shukurov A., Snodin A. P., Seta A., Bushby P. J., Wood T. S., 2017, *Astrophys. J. Lett.*, **839**, L16
- Sokoloff D. D., Bykov A. A., Shukurov A., Berkhuijsen E. M., Beck R., Poezd A. D., 1998, *Mon. Not. R. Astron. Soc.*, **299**, 189
- Squire J., Hopkins P. F., 2017, *Mon. Not. R. Astron. Soc.*, **471**, 3753
- Subramanian K., 1999, *Phys. Rev. Lett.*, **83**, 2957
- Subramanian K., 2003, *Phys. Rev. Lett.*, **90**, 245003
- Subramanian K., 2016, *Reports on Progress in Physics*, **79**, 076901
- Sutherland R. S., Dopita M. A., 1993, *ApJS*, **88**, 253
- Tritsis A., Panopoulou G. V., Mouschovias T. C., Tassis K., Pavlidou V., 2015, *Mon. Not. R. Astron. Soc.*, **451**, 4384
- van de Voort F., Bieri R., Pakmor R., Gómez F. A., Grand R. J. J., Marinacci F., 2021, *Mon. Not. R. Astron. Soc.*, **501**, 4888
- Vainshtein S. I., Zel'dovich Y. B., 1972, *Soviet Physics Uspekhi*, **15**, 159
- Vázquez-Semadeni E., 1994, *Astrophys. J.*, **423**, 681
- Vázquez-Semadeni E., Gómez G. C., Jappsen A. K., Ballesteros-Paredes J., González R. F., Klessen R. S., 2007, *Astrophys. J.*, **657**, 870
- Waagan K., Federrath C., Klingenberg C., 2011, *J. Comput. Phys.*, **230**, 3331
- Yang Y., Wan M., Matthaeus W. H., Shi Y., Parashar T. N., Lu Q., Chen S., 2019, *Physics of Plasmas*, **26**, 072306
- Yuen K. H., Lazarian A., 2020, *Astrophys. J.*, **898**, 66
- Zel'dovich Ya. B., Ruzmaikin A. A., Molchanov S. A., Sokoloff D. D., 1984, *Journal of Fluid Mechanics*, **144**, 1
- Zweibel E. G., 2017, *Physics of Plasmas*, **24**, 055402

## APPENDIX A: VARYING THE COOLING IMPLEMENTATION

In our simulations, the time step is primarily decided based on the following three physical processes: fastest speed ( $dt_{\text{MHD}}$ , Eq. A1), fastest heating or cooling, ( $dt_{\text{cool}}$ , Eq. A2), and the diffusion of velocity and magnetic fields ( $dt_{\text{diff}}$ , Eq. A3). They are given by

$$dt_{\text{MHD}} = \text{CFL}_{\text{coeff}} \frac{dx}{\text{MAX} \left( \left( u^2 + c_s^2 + v_A^2 \right)^{1/2} \right)}, \quad v_A = \frac{b}{\sqrt{4\pi\rho}}, \quad (\text{A1})$$

$$dt_{\text{cool}} = \text{ssf} \frac{e_{\text{int}}}{n_{\text{H}}^2 \Lambda(T) - n_{\text{H}} \Gamma}, \quad (\text{A2})$$

$$dt_{\text{diff}} = \frac{1}{2} \frac{(dx)^2}{\text{MAX}(v, \eta)}, \quad (\text{A3})$$

where  $\text{CFL}_{\text{coeff}}$  is the coefficient for the Courant - Friedrichs - Lewy (CFL) condition (chosen to be 0.6 throughout),  $dx$  is the grid resolution,  $u$  is the gas speed,  $c_s$  is the sound speed,  $v_A$  is the Alfvén speed,  $b$  is the magnetic field,  $\rho$  is the density,  $\text{ssf}$  is the subcycling safety factor,  $e_{\text{int}}$  is the internal energy,  $n_{\text{H}}$  is the number density ( $= \rho/\mu m_{\text{H}}$ , where  $\mu = 1$  is the mean molecular weight and  $m_{\text{H}}$  is the mass of hydrogen),  $\Lambda$  is the cooling function (Eq. 6),  $\Gamma$  is the heating function (Eq. 5),  $v$  is the viscosity,  $\eta$  is the resistivity and the function  $\text{MAX}$  returns the maximum of a quantity within the domain (in Eq. A1) or among a list of variables (in Eq. A3). One would naturally expect the time step to be minimum of all three time steps (Eq. A1 – Eq. A3) but  $dt_{\text{cool}}$  can be quite small in comparison to other two time steps. This can be numerically very expensive, especially for our dynamo runs as the simulations usually runs over  $\gtrsim 100$  eddy turnover times.

In our simulations, we treat the cooling and heating functions as a source term in an operator split fashion, i.e., after every time step  $= \text{MIN}(dt_{\text{MHD}}, dt_{\text{diff}})$ , we update the internal energy to reflect the corresponding cooling and heating. For the equilibrium cooling model, we first obtain an equilibrium temperature by balancing the heating and cooling functions ( $\Gamma = n_{\text{H}}\Lambda$ ). Then if the time taken to achieve the equilibrium temperature from the temperature at that time is less than  $dt_{\text{cool}}$  (with  $\text{ssf} = 1$ ), then the temperature is made to approach the equilibrium temperature exponentially fast (Vázquez-Semadeni et al. 2007). If not, the cooling and heating is performed according to the time step.

We also try the non-equilibrium cooling model, where we update



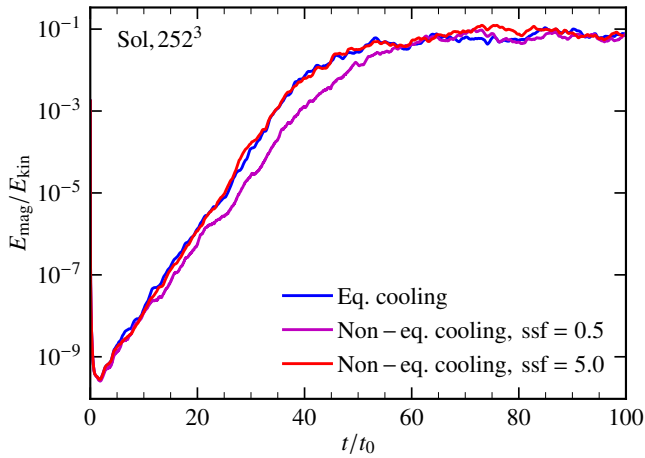


**Figure A1.** The ratio of the magnetic to turbulent kinetic energy,  $E_{\text{mag}}/E_{\text{kin}}$ , for two different cooling models: equilibrium cooling (Eq. cooling) and non-equilibrium cooling (Non – eq. cooling, with two different  $\text{ssf}$ , 0.5 and 5.0). There is a slight variation in the curve for Non – eq. cooling,  $\text{ssf} = 0.5$  case but the overall growth rate and saturation level do not depend on the cooling implementation.

the internal energy according the cooling time step,  $dt_{\text{cool}}$  (with  $\text{ssf} = 0.5$  and 5.0). Here, for each spatial cell, we evolve the internal energy in steps of  $dt_{\text{cool}}$  and this can be different for different cells (also see Sec. 2.2.5 in Mohapatra et al. 2022b). We compare the runs with the equilibrium and non-equilibrium cooling (two different  $\text{ssf}$ , 0.5 and 5.0) models for the purely solenoidal driving (Sol) and  $252^3$  grid points (other parameters stay the same as in Sec. 2). In Fig. A1, we show the ratio of the magnetic to turbulent kinetic energy, which has a slight deviation for the non-equilibrium cooling model with  $\text{ssf} = 0.5$  but the overall growth rate and saturation level are not affected much. In Fig. A2, we show the PDF of density and temperature for all three cases and they are roughly equal in all three cases. Thus, we conclude that the properties of the multiphase medium and the magnetic field it amplifies do not depend on the exact way the cooling and heating is implemented and we adopt the equilibrium cooling model for our runs to maximise numerical efficiency.

## APPENDIX B: PROBABILITY DISTRIBUTION FUNCTIONS OF VELOCITY AND LOCAL MACH NUMBER

Fig. B1 (a, b) shows 2D PDFs of velocity and density for both the Sol and Comp runs. For both cases, the velocity shows a very low level negative correlation (practically uncorrelated) with the density and this is true in all the phases. Fig. B1 (c, d) shows the PDF of the velocity component,  $u_x/u_{\text{rms}}$ ,  $T \geq 0$  K, for both the Sol and Comp cases in different phases. Like the density (Fig. 4), the velocity PDF does not vary significantly between the kinematic and saturated stages. The velocity PDF always roughly follows a Gaussian distribution with a mean approximately equal to zero in all the phases and for both the cases. The standard deviation of the velocity PDF is higher for the Comp case as the density varies over a larger range for that case (Fig. 4). For both cases, the standard deviation is higher in the  $T \geq 10^3$  K phase due to lower densities.

The correlation of Mach number with density is more significant. Fig. B2 shows 2D PDFs of the local Mach number ( $\mathcal{M}_{\text{local}} = u_{\text{rms}}/c_s$ ,

computed at each point locally) and density for both runs. In both cases, the correlation is positive and stronger for the  $T < 10^3$  K phase and weakens for the  $T \geq 10^3$  K phase. These results are different from those in Federrath & Banerjee (2015), which shows a negative  $\mathcal{M}_{\text{local}} - \rho$  correlation (see their Fig. 7) for turbulence driven in a gas with a polytropic equation of state and  $\gamma_g = 5/3$ . This is probably due to the multiphase nature of the medium in our simulations. Fig. B2 (c, d) shows PDF of  $\log(\mathcal{M}_{\text{local}})$  for both Sol and Comp runs. Overall ( $T \geq 0$  K region), like density PDFs in Fig. 4, show a double hump structure in both cases confirming the two-phase nature of the gas. Though the rms Mach number,  $\mathcal{M}$  (Fig. 7 (e, f)), in the  $T < 10^3$  K phase is  $\approx 5$  and that in the  $T \geq 10^3$  K phase is  $\approx 1$ ,  $\mathcal{M}_{\text{local}}$  in both phases varies over a huge range and there is significant overlap (especially at lower  $\mathcal{M}_{\text{local}}$ ) between the PDFs in the two phases.

## APPENDIX C: CURVATURE OF MAGNETIC FIELD LINES

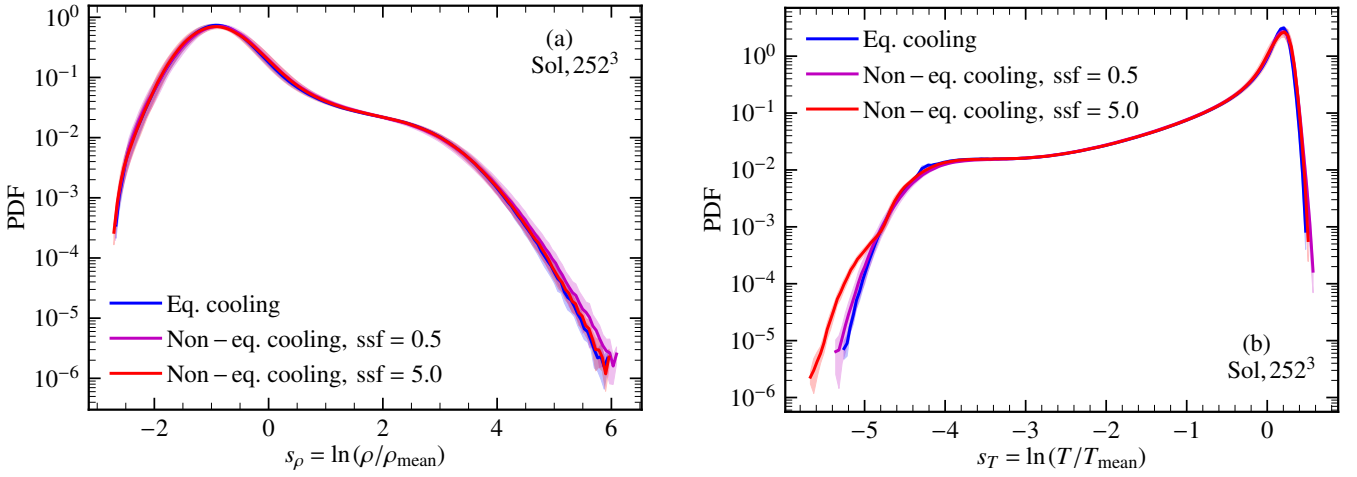
The magnetic field structure is also expected to be different in different phases of the ISM. In this work too, the local magnetic field structure varies between the  $T < 10^3$  K and  $T \geq 10^3$  K phases. This is confirmed via various direct and indirect measures shown in the main text, especially via  $b$ - $\rho$  2D PDFs (Fig. 5),  $b_x/b_{\text{rms}}$  PDFs (Fig. 6), and the time evolution of the Lorentz force (Fig. 12). We characterise the local magnetic field structure in terms of curvature of magnetic field lines, usually defined by  $|\hat{b} \cdot \nabla \hat{b}|$ , where  $\hat{b} = \mathbf{b}/\|\mathbf{b}\|$  denotes the magnetic field unit vector (Schekochihin et al. 2004).

In numerical simulations,  $\hat{b} \cdot \nabla \hat{b}$  need not be perpendicular to  $\hat{b}$  (primarily due to numerical error in computing the gradient) and the curvature,  $\kappa$ , can be more accurately computed as (Yang et al. 2019; Yuen & Lazarian 2020)

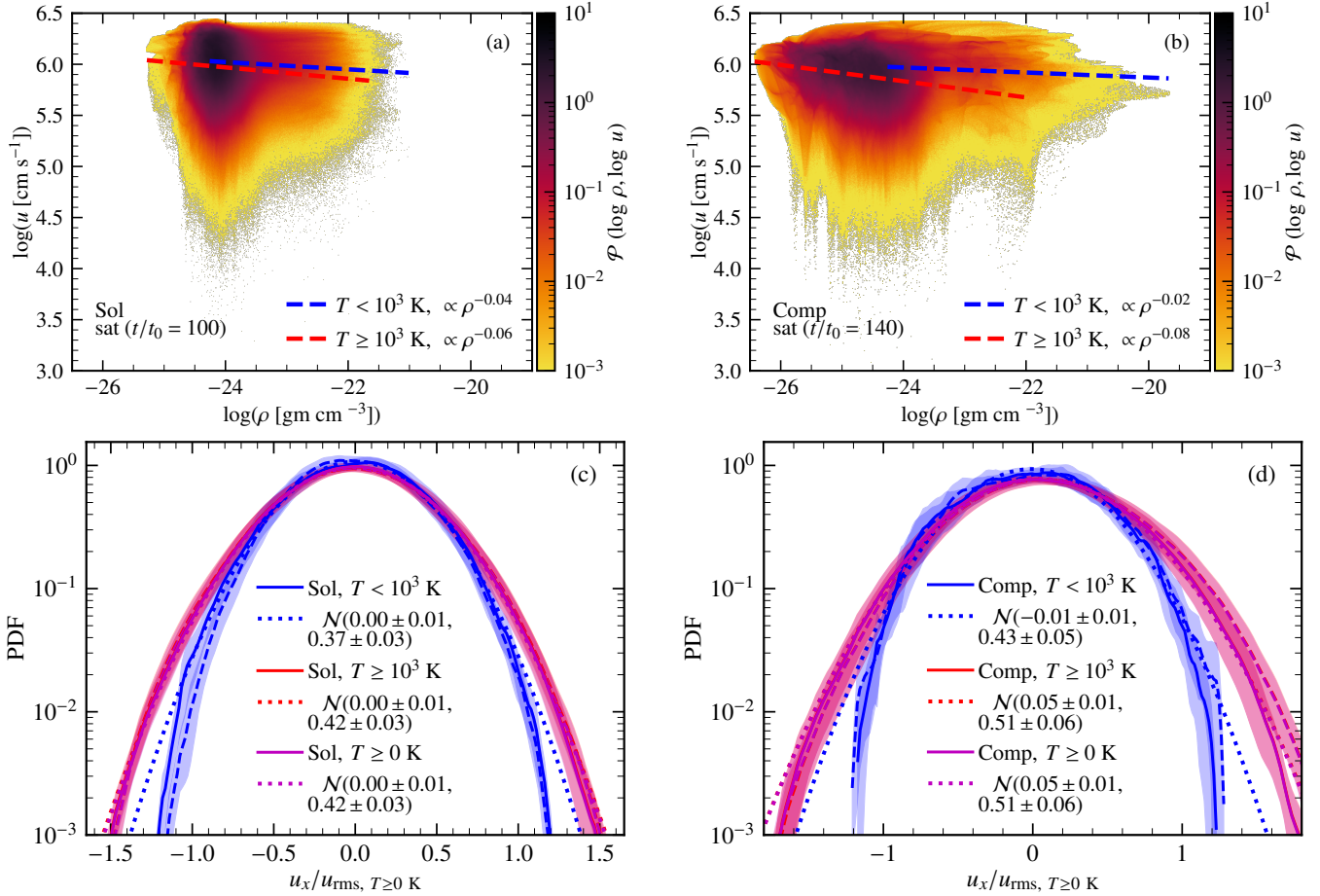
$$\kappa = \| \hat{b} \times (\hat{b} \cdot \nabla \hat{b}) \|. \quad (\text{C1})$$

Fig. C1 shows the time evolution of rms curvature,  $\kappa_{\text{rms}}$ , in all the phases for both the Sol and Comp runs. For both runs, the curvature is higher in the  $T < 10^3$  K phase in comparison to the  $T \geq 10^3$  K phase and decreases for both phases as the magnetic field saturates (the level of decrease is lower for the Comp run). This indicates slightly more tangled magnetic field lines in the  $T < 10^3$  K phase and the kinematic stage for both types of driving. Also, since the values are always higher for the Sol case, the magnetic field lines are more tangled for the purely solenoidal driving in comparison to the purely compressive driving.

This paper has been typeset from a  $\text{\LaTeX}$  file prepared by the author.



**Figure A2.** PDFs of density,  $s_\rho = \ln(\rho/\rho_{\text{mean}})$  (a) and temperature,  $s_T = \ln(T/T_{\text{mean}})$  (b) for Eq. cooling (blue), Non-eq. cooling,  $\text{ssf} = 0.5$  (magenta) and Non-eq. cooling,  $\text{ssf} = 5.0$  (red) in the kinematic stage. The solid lines show the PDF averaged over 20 independent eddy turnover times ( $t/t_0 = 10 - 30$  in Fig. A1) and the shaded region shows one-sigma variation. There is slight variation at lower temperatures but both the density and temperature PDFs practically overlap for all three cases.



**Figure B1.** 2D PDFs of velocity and density for the Sol (a) and Comp (b) runs with colour showing the corresponding probability. The coloured lines show the trends for  $T < 10^3$  K (blue),  $T \geq 10^3$  K (red), and  $T \geq 0$  K (magenta) phases. For both runs in all phases, velocity-density shows very low level negative correlation (practically uncorrelated). PDF of the velocity component,  $u_x/u_{\text{rms}, T \geq 0 \text{ K}}$  for both Sol (c) and Comp (d) runs with colours showing different phases. These PDFs roughly follow a Gaussian distribution,  $\mathcal{N}(\text{mean}, \text{standard deviation})$ , with mean  $\approx 0$  and a standard deviation which slightly higher in the  $T \geq 10^3$  K phase (due to lower densities) and for the Comp case (due to a broader density distribution, see Fig. 4).

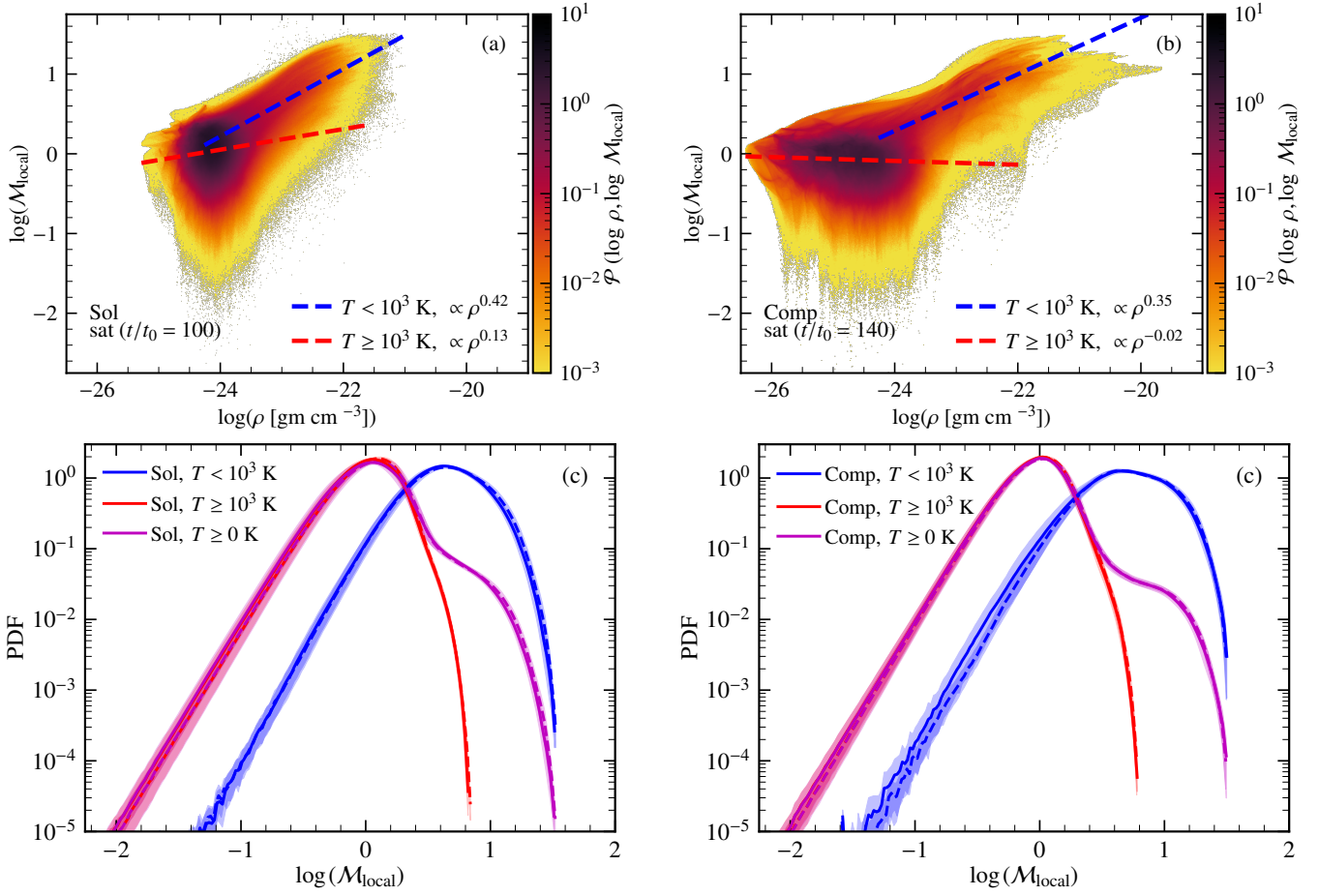


**Figure B2.** Same as Fig. B1 but for the local Mach number,  $M_{\text{local}} (= u_{\text{rms}}/c_s$  at each point locally).  $M_{\text{local}}-\rho$  shows stronger positive correlation in the  $T < 10^3$  K phase and the correlation decreases significantly in the  $T \geq 10^3$  K phase (a, b). Like the density PDFs in Fig. 4, the PDF of  $\log(M_{\text{local}})$  for  $T \geq 0$  K region shows a double hump structure for both cases, re-confirming the two-phase nature of the medium. Though the rms Mach number,  $\mathcal{M}$ ,  $\approx 5$  in the  $T < 10^3$  K phase and  $\approx 1$  in the  $T \geq 10^3$  K phase (Fig. 7 (e, f)),  $M_{\text{local}}$  varies over a huge range in both the phases for both the Sol and Comp runs and there is a significant overlap between the PDFs in two phases.

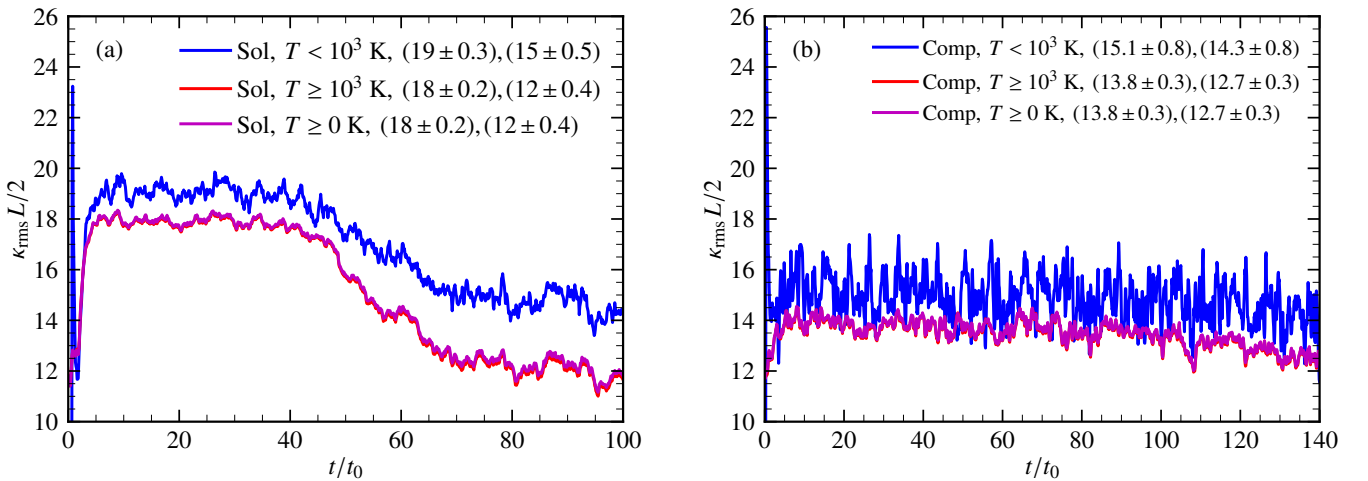


**Figure C1.** Time evolution of the rms curvature,  $\kappa_{\text{rms}}$ , normalised by driving scale of turbulence ( $L/2$ , see Sec. 2.3) for both the Sol (a) and Comp (b) runs in all three phases:  $T < 10^3$  K (blue),  $T \geq 10^3$  K (red), and  $T \geq 0$  K (magenta). The corresponding time-averaged values in the kinematic and saturated stages for each case are given in the legend. Practically, the line for the  $T \geq 10^3$  K phase (filling most of the volume) overlaps with that for the whole region. For both runs, the magnetic field line curvature is higher for the  $T < 10^3$  K phase and decreases on saturation. Also, the curvature is always higher for the Sol case in comparison to the Comp case.